MNRAS 000, 1–24 (2025) Preprint 27 November 2025 Compiled using MNRAS LATEX style file v3.2

Deep Extragalactic VIsible Legacy Survey (DEVILS): First Data Release Covering The D10 (COSMOS) Region

L. J. M. Davies[1★], M. Bravo[2], R. H. W. Cook[1], A. Hashemizadeh[1], J. E. Thorne[1], S. Bellstedt[1], S. P. Driver[1], A. S. G. Robotham[1], S. Koushan[1], N. Adams[3], S. Huynh[4], E. J. A. Mannering[4], J. Tocknell[4], M. J. I. Brown[5], J. Bland-Hawthorn[6], L. Cortese[1], B. Catinella[1], M. Meyer[1], S. Phillipps[7], M. Siudek[8,9], C. Wolf[10]

[1] ICRAR, The University of Western Australia, 35 Stirling Highway, Crawley, WA 6009, Australia
[2] Department of Physics & Astronomy, McMaster University, 1280 Main Street W, Hamilton, ON, L8S 4M1, Canada
[3] Jodrell Bank Centre for Astrophysics, University of Manchester, Oxford Road, Manchester M13 9PL, UK
[4] Australian Astronomical Optics, Macquarie University, Sydney, NSW, Australia
[5] School of Physics & Astronomy, Monash University, Clayton, VIC, Australia
[6] Sydney Institute for Astronomy, School of Physics, A28, The University of Sydney, NSW 2006, Australia
[7] Astrophysics Group, School of Physics, University of Bristol, Bristol BS8 1TL, UK
[8] Instituto de Astrofísica de Canarias, Vía Láctea, 38205 La Laguna, Tenerife, Spain
[9] Instituto de Astrofísica de Canarias (IAC); Departamento de Astrofísica, Universidad de La Laguna (ULL), 38200, La Laguna, Tenerife, Spain
[10] Research School of Astronomy and Astrophysics, Australian National University, Canberra, ACT 2611, Australia

Accepted XXX. Received YYY; in original form ZZZ

ABSTRACT

The Deep Extragalactic VIsible Legacy Survey (DEVILS) is a deep, high-completeness multi-wavelength survey based around spectroscopic observations using the Anglo-Australian Telescope's AAOmega spectrograph. The survey covers $\sim 4.5\,\mathrm{deg}^2$ over three extragalactic fields to $\mathrm{Y}_{AB} < 21.2$ mag and probes sources at $0 < z < 1.2$, with a median redshift of $z = 0.53$. Here we describe the DEVILS spectroscopic observations, data reduction and redshift analysis. We then describe and release to the community all DEVILS data in the 10h (D10, COSMOS) region including: i) catalogues of redshifts, photometry, SED fitting for physical properties, visual morphologies, structural decompositions and group environments/halo masses, ii) matched imaging in 28 bands from x-rays to radio continuum, and iii) reduced 1D spectra. All data are made publicly available through `Data Central`†. Within D10 we obtain 5,442 new high-quality spectroscopic redshifts. When combined with existing, lower-quality, redshift information (*i.e.* photometric redshifts) this is increased to 7,946. Of these, 3,122 have a spectroscopic redshift from another source (many that was not available at the time of the DEVILS observations). As such, DEVILS provides new unique high-quality spectroscopic redshifts for 4,824 faint sources in COSMOS. This increases the spectroscopic completeness at Y-mag∼21 from ∼50% in other samples to ∼90% in DEVILS. Finally, we show the power of this dataset by exploring the suppression of star formation in over-dense environments, split by morphology and stellar mass, and highlighting the ubiquitous nature of environmental quenching.

Key words: methods: observational, techniques: spectroscopic, surveys, catalogues, galaxies: evolution, galaxies: star formation

1 INTRODUCTION

Over the last few decades large multi-object spectroscopic galaxy evolution-focused surveys have revolutionised our understanding of the processes which shape the Universe we live in today. These surveys have now allowed us to explore the properties of over a million galaxies covering a range of epochs and perform statistical analyses to identify the most significant drivers in the galaxy evolution process (*e.g.* Kauffmann et al. 2003b; Lewis et al. 2002b; Peng et al. 2010; Taylor et al. 2011). These studies have uncovered a wealth of information, suggesting that galaxy evolution is a complex and multi-faceted process, being driven by many co-dependant and overlapping factors, such as age, stellar mass, metallicity, available gas supply, star-formation rate, morphology, active galactic nuclei, mergers, interactions, and larger-scale environmental effects, to mention but a few.

Given the complex nature of the galaxy evolution process, larger and most robustly parameterised galaxy samples allow us to better constrain this complex web of processes by both improving number statistics and allowing us to more-finely subdivide galaxies based on their characteristics, while still retaining adequate statistically-significant sample sizes (*e.g.* see Driver et al. 2022a). However, care must be taken as sample biases can plague our understanding of the

★ E-mail: luke.j.davies@uwa.edu.au
† `datacentral.org.au`

core mechanisms which shape galaxy evolution. Primarily three biases can lead misinterpretation of results: i) sample incompleteness in any one of the properties being studied can lead to interpretation biases (*e.g.* see Cameron & Driver 2007), particularly when controlling for one observable to explore another (*e.g.* controlling for stellar mass, to explore another property, when the sample is incomplete in stellar mass), ii) observational accuracy limitations (for example, fundamental limitations in a particular survey's ability to measure galaxy properties due to limited signal-to-noise spectra or photometric bands) and iii) progenitor bias, where it is problematic to compare similar galaxy populations over a range of epochs (*e.g.* see van Dokkum & Franx 1996; Belli, Newman, & Ellis 2015). The latter can lead to significant biases when exploring evolutionary trends. Many surveys aim to correct for one or more of these three effects to better constrain observational galaxy evolution studies, with varying degrees of success.

Historically, galaxy evolution-focused surveys have fallen into two broad classes, largely driven by observational limitations. The first targets large volumes of the local (z<0.2) Universe to high spatial and spectroscopic completeness, aiming to reduce sample incompleteness by targeting a significant fraction of the galaxy population over a fixed volume and down to a limiting observational brightness/magnitude. Surveys such as the Sloan Digital Sky Survey (SDSS, *e.g.* Abazajian et al. 2009), the Two Degree Field Galaxy Redshift Survey (2dFGRS, Colless et al. 2001), Galaxy And Mass Assembly Survey (GAMA, Driver et al. 2011; Liske et al. 2015) and more recently the Dark Energy Spectroscopic Survey Bright Galaxy Sample (DESI-BGS, Hahn et al. 2023) have revolutionised our view of the local Universe.

To mention just a few key areas, they have transformed our understanding the dark matter distribution on scales of a few kpc to >1 Mpc (*e.g.* Peacock et al. 2001; Robotham et al. 2011; Yang et al. 2007; Tempel et al. 2014a; Alam et al. 2017; Driver et al. 2022b), the effect of both large-scale environment (*e.g.* Lewis et al. 2002a; Peng et al. 2010; Alpaslan et al. 2015) and local environment (Patton et al. 2011; Knobel et al. 2015; Davies et al. 2015b, 2016, 2019b) on galaxy evolution, allowed an exploration of the low stellar mass Universe (*e.g.* Baldry et al. 2010; Wright et al. 2017), explored fundamental relations linking galaxy stellar mass, star-formation and metallically (*e.g.* Kauffmann et al. 2003a; Tremonti et al. 2004; Brinchmann et al. 2004; Gunawardhana et al. 2011; Davies et al. 2016b), determined the impact of active galactic nuclei on galaxy properties (*e.g.* Kauffmann et al. 2003b; Gadotti & Kauffmann 2009b), and linked morphological and structural parameters with key evolutionary mechanisms (*e.g.* Gadotti 2009a; Kelvin et al. 2012; Lange et al. 2015; Driver et al. 2022a). While these surveys have proved invaluable in parameterising the local galaxy population, they are limited in measuring the astrophysics that led to their formation - *i.e.* using these surveys we are witnessing the in-situ processes that are driving galaxy evolution right now, but are limited in our ability to understand the mechanisms that have led to the $z\sim0$ galaxy population over the last $\sim$ 10 Gyrs of Universal history.

The second class of galaxy evolution-focused surveys have aimed to address this by targeting smaller areas but fainter sources, extending out into the distant Universe. Surveys such as zCOSMOS (Lilly et al. 2007), the Very Large Telescope (VLT) VIsible Multi-Object Spectrograph (VIMOS) Deep Survey (VVDS, Le Fèvre et al. 2013), VIMOS Ultra-Deep Survey (VUDS, Le Fèvre et al. 2015), VIMOS Public Extragalactic Redshift Survey (VIPERS, Garilli et al. 2014) and DEEP2/3 (Cooper et al. 2012; Newman et al. 2013) have explored earlier epochs ($z>0.5$), probing earlier stages of galaxy evolution. However, due to observational limitations in parameterising faint sources, these surveys typically trade off spectral completeness for sample size, sparse-sampling the galaxy population at a given epoch. While this approach does not inhibit these surveys' specific science goals, it does lead to increased sample bias, which then needs to be corrected for when exploring the evolution of galaxy properties. This is particularly true when studying the environmental impact on galaxy properties, where environmental metrics on group- and merger-scales (*i.e.* sub-Mpc) are very sensitive to small-scale spatial and spectral incompleteness (Robotham et al. 2011; Tempel et al. 2014b, 2017). On these scales, dark matter haloes virialize and merge, and gas collapses to form galaxies. Thus, this regime is paramount to our understanding of baryon physics, and the interplay between dark matter and directly-observable galaxy components. To study sub-Mpc scales spectroscopic completeness is key, as even the most high fidelity photometric redshifts are not precise enough to identify these structures.

Within the Deep Extragalactic VIsible Legacy Survey (DEVILS Davies et al. 2018, 2021) we aim to combine the two approaches detailed above, producing a deep magnitude-limited (Y<21.2 mag), but also high spectral and spatial completeness (> 85%) spectroscopic survey of three well-established legacy fields: XMM-Newton Large-Scale Structure field (XMM-LSS), Extended Chandra Deep Field-South (ECDFS), and Cosmological Evolution Survey field (COSMOS). DEVILS is designed to detect down to the stellar masses of $M^*_{z=0}$ galaxies to $z=1$ ($10^{10.8}\,M_\odot$ - the typical galaxy in the local Universe in terms of mass-density budget, Wright et al. 2017), major merger pairs of $M^*_{z=0}$ galaxies to $z\sim0.5$, and groups down to $10^{13}\,M_\odot$ to $z=0.5$. The approach, science goals and target selection for DEVILS are described extensively in Davies et al. (2018). However, we note here that the key focus of the DEVILS survey is to explore the group-scale environment and its impact on galaxy evolution at intermediate redshift.

The survey is also specifically designed to match the GAMA sample in a number of key respects, but to extend out to the more distant Universe - allowing us to define comparable samples of galaxies across a broad evolutionary range with minimal selection and measurement biases. Briefly, within GAMA and DEVILS we define input catalogues using similar imaging (see Bellstedt et al. 2020a; Davies et al. 2021) and the same photometric codes (Robotham et al. 2018), observe spectra using the same instrument+facility (the AAOmega Spectrograph on the Anglo-Australian Telescope, AAT) and observational/reduction set-up, measure redshifts using the same methodology (Baldry et al. 2014), measure galaxy properties such as stellar mass, star formation rate (SFR) and star-formation histories (SFH) using the same methodology (Robotham et al. 2020; Bellstedt et al. 2020b; Thorne et al. 2021), and define environmental metrics such as nearest-neighbour density (Davies et al. 2025d) and group/cluster properties (Robotham et al. 2011; Bravo et al. 2025) using the same approach. In combination this minimises selection and measurement biases across the two surveys allowing us to directly compare galaxies and environments across a large evolutionary baseline (also aiming to minimise progenitor bias). DEVILS also serves as a precursor to the upcoming 4m Multi-Object Spectrograph Telescope (4MOST, de Jong et al. 2019) Wide Area Vista Extragalactic Survey (WAVES, Driver et al. 2019) deep program, which will target similar galaxy populations but covering a much larger area. As such, the DEVILS data can be used to plan data collection and science exploitation for WAVES. What's more, in the near future there will be deluge of surveys probing high-completeness samples of galaxies outside of the local Universe from facilities such a William Hershel Telescope's Enhanced Area Velocity Explorer (WEAVE, Jin et al. 2024), Subaru's Prime Focus Spectrograph (PFS, Greene et al. 2022), the

Very Large Telescope's Mulit-Object Optical and Near-IR Spectrograph (MOONS, Cirasuolo et al. 2020) and ultimately with the European Southern Observatory's proposed Wide-field Survey Telescope (WST, Mainieri et al. 2024). Thus, the DEVILS dataset represents a timely comparison point for all of these upcoming surveys.

The DEVILS team have already published a number of key science and technical papers exploring the extragalactic background light (Koushan et al. 2021), the evolution of galaxy morphology (Hashemizadeh et al. 2021) and structure (Hashemizadeh et al. 2022; Cook et al. 2025), the evolution of star-formation and stellar mass (Thorne et al. 2021; Davies et al. 2022), the evolution of the SFR-mass-metallicity relation (Thorne et al. 2022), the evolution of cosmic star-formation and AGN activity (D'Silva et al. 2023), SFR timescales using deep radio continuum imaging (Cook et al. 2025), robust galaxy merger rates at intermediate redshift (Fuenblackba-Fuentes et al. 2025), the evolution of the star-forming sequence using recent SFHs (Davies et al. 2025a), the impact of AGN feedback in galaxy quenching (Davies et al. 2025b), the environmental quenching of satellites at intermediate redshifts (Davies et al. 2025c) and the evolution of the morphology-density relation (Davies et al. 2025d). In this work we now present the first public data release of the DEVILS sample used in the majority of these works. This includes all observed and derived properties in the D10/COSMOS region, including catalogues of photometric measurements, redshifts, SED fit parameters, visual morphological classifications, structural decomposition parameters, and group environmental diagnostics, standardised imaging covering 28 bands in the D10 regions, and standardised 1D spectroscopic data in the D10 region from our DEVILS observations at the AAT, zCOMSOS and DESI for DEVILS sources. All data is made available to the community via the `Data Central` web portal: `datacentral.org.au` to allow further scientific exploration outside of the core DEVILS team. In this paper, we detail the DEVILS target catalogue (Section 2), spectroscopic observations and data reduction at the AAT (Section 3), sample diagnostics in the D10 region (including comparisons to existing samples, Section 5), the compilation of the master D10 redshift catalogue (Section 6), and details of all data products provided in this release (Section 7). We finish by highlighting the power of this sample (in addition to existing DEVILS papers) by exploring the impact of local galaxy density on star-formation, when controlled for stellar mass and morphology (Section 8).

2 TARGET CATALOGUE

The DEVILS regions and target catalogues are described extensively in Davies et al. (2018), as such we only briefly summarise the key points here. In all DEVILS regions VISTA Y-band imaging is used for our base target selection. Public imaging in the D10 region is taken from the Ultra-deep Visible and Infrared Survey Telescope for Astronomy (VISTA) survey (UltraVISTA, McCracken et al. 2012) and VISTA Deep Extragalactic Observations survey (VIDEO, Jarvis et al. 2013). Source photometry is measured using the ProFound code (Robotham et al. 2018) which identifies peak flux positions within the image, performs watershed deblending to identify source segments and then iteratively grows (dilates) these segments to measure both total and colour-optimised photometry. These measurements and associated flags are all provided in the DEVILS DR1 data release within the `devils_dr1.D10ProFoundPhotometry` catalogue. The input imaging bands used to derive the DEVILS photometry, are also provided via `Data Central` (`datacentral.org.au`).

For the flags, we use the ProFound NIR photometric measurements to perform star-galaxy separations based on NIR colour and source size. Sources classified as galaxies are assigned `starFlag=0`, stars assigned `starFlag=1` and ambiguous objects `starFlag=2`. Next, we use the ProFound output to produce a star and artefact mask. We retain all ProFound sources in our catalogues, but sources in unmasked regions are assigned `mask=0`, while sources in masked regions have `mask>0` (with the number indicating the reason the sources was masked and details of these flags are provided in the catalogue). Finally, using ProFound outputs for source colours and sizes we apply an additional artefact flag for a small number of objects that may have been missed in the masking process. These are assigned flags of `artefactFlag=0` (not an artefact) and `artefactFlag=1` (is likely an artefact). As such, to build a sample of galaxies with robust photometric measurements from the DEVILS DR1 catalogues, a user would apply the filter: `mask=0` & `starFlag=0` & `artefactFlag=0`. The imaging data, photometric measurements and star-galaxy separation, masking and artefact flagging are described extensively in Davies et al. (2018) and Davies et al. (2021). As such, we refer the reader to these works for further information.

To build the DEVILS target catalogue for spectroscopic observations, we take all sources selected as galaxies in unmasked regions of our field with total magnitudes of $Y_{AB} < 21.2$mag. First, the left panel of Figure 1 shows the Y magnitude vs observed-frame *g*-*i* colour for all of these targets, while in the right panel we show the same but coloured by pre-DEVILS redshift completeness. Targets without an existing spectroscopic redshift are typically faint, but span a broad range of rest-frame colours. In existing spectroscopic samples, there is a higher fraction of blue galaxies have a spectroscopic redshift as we move to fainter magnitudes. This is expected as blue galaxies typically have nebular emission lines, for which redshifts are more easily obtained.

Next, considering the spatial distribution of targets, the left panel of Figure 2 shows the target density across the D10 region, where masked regions are displayed as white spaces. In the right panel of Figure 2 we show the pre-DEVILS photometric redshift distribution of our targets taken from the COSMOS2015 catalogue (Laigle et al. 2016). This results in 17,209 possible un-masked, extragalactic targets in the D10 region.

In a final step we removed objects with an existing high-confidence, spectroscopic redshift (at the time of DEVILS observations) to maximise the scientific return from our observations. These sources are described extensively in section 5.1.1 of Davies et al. (2018), but we note here that we remove sources with high-confidence redshifts from VVDS (Le Fèvre et al. 2014), zCOSMOS (Lilly et al. 2007), VUDS (Le Fèvre et al. 2013) and hCOSMOS (Damjanov et al. 2018). Redshifts from all other programs are included in our target catalogue. We find that of our full target catalogue 7,980 sources have an existing high confidence spectroscopic redshift, leaving 9,229 targets with unknown or un-secure redshifts in the field. We then also re-observe a random subsample of zCOSMOS (627) and hCOMOS (303) covering a range of redshifts and magnitudes with which to compare our DEVILS-AAT redshifts. These targets are included in our input catalogue, resulting in a total target sample of 10,159 sources. In our master redshift compilation (see Section 6), we include all of the existing redshifts to form our highly-spectroscopically complete sample.

3 SPECTROSCOPIC OBSERVATIONS

DEVILS spectroscopic observations were undertaken at the 3.9m Anglo-Australian telescope at the Siding Spring Observatory in New

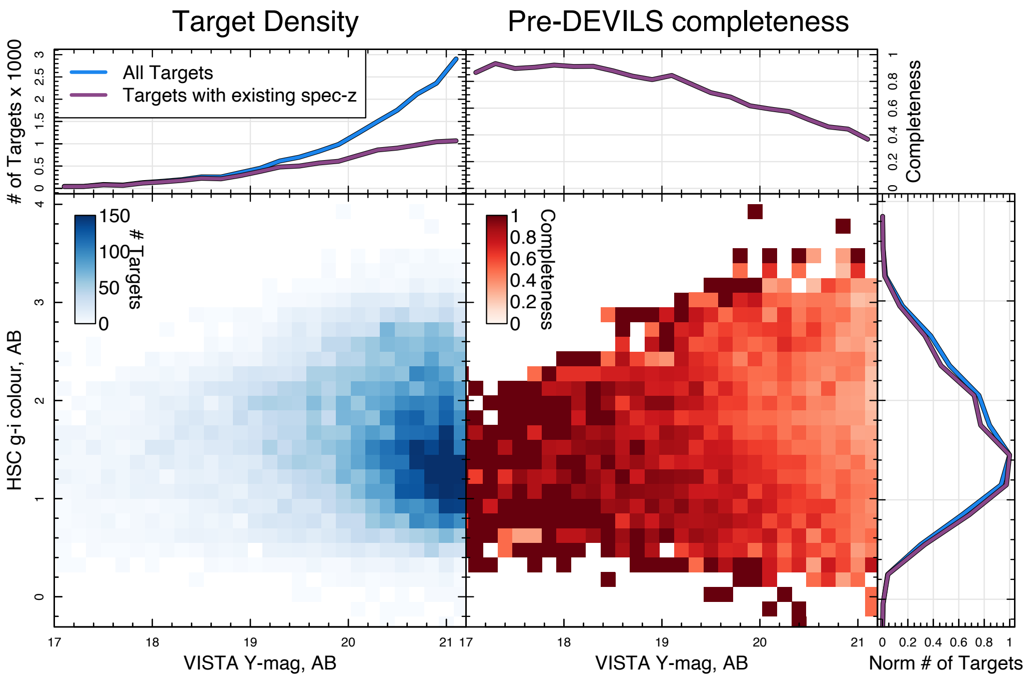

Figure 1. Left: The colour-magnitude density of all targets in the D10 region. Right: The colour-magnitude completeness of sources with pre-DEVILS robust spectroscopic redshifts. Targets without a spectroscopic redshift are typically faint, but span a broad range of rest-frame colours. In existing spectroscopic samples, there is a higher fraction of blue galaxies that have a spectroscopic redshift at faint magnitudes - as expected.

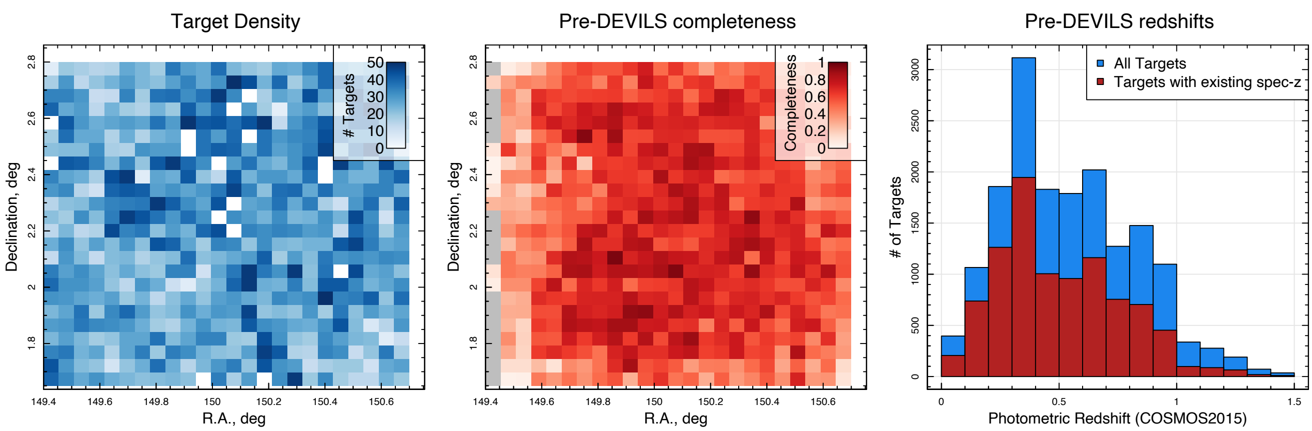

Figure 2. Left: The spatial source density of targets in the D10 region. Middle: The spatial completeness of sources with pre-DEVILS robust spectroscopic redshifts - completeness is patchy and higher in the central region of the field. Right: The pre-DEVILS photometric redshift distribution of targets in the D10 region taken from Laigle et al. (2016), all targets are shown in blue, and those with a pre-DEVILS robust spectroscopic redshifts shown in red. Pre-DEVILS completeness to our target sample is ∼ 0.5 at all redshifts.

South Wales with the AAOmega fibre-fed spectrograph (Saunders et al. 2004; Sharp et al. 2006) in conjunction with the Two-degree Field (2dF, Lewis et al. 2002a) positioner. The 2dF positioner has been at the forefront of large galaxy redshift surveys in the local Universe (such as 2dFGRS and GAMA) and has also been used to great success in targeting large numbers of sources to higher redshift (*e.g.* 2dFLenS and WiggleZ, Blake et al. 2016; Drinkwater et al. 2018) and more recently to faint magnitudes (OzDES, Childress et al. 2017). As such, it is an ideal facility to perform our deep intermediate redshift survey. 2dF allows the simultaneous observation of ∼ 400 targets with the AAOmega spectrograph, with 2′′ diameter fibres. The 2dF top-end consists of an atmospheric dispersion compensator (ADC) and robot gantry that positions fibres to 0.3′′ accuracy on sky.

AAOmega observes in two spectral channels (blue and red), both equipped with a 2k×4k E2V CCD detector and an AAO2 CCD controller. We observed with the 5700Å dichroic allowing for simultaneous coverage from 3750Å to 8850Å. For the blue CCD we use the 580V grating with central wavelength of 4820Å providing a ∼ 1.03Å/pix dispersion, while for the red CCD we use the 385R grating with central wavelength of 7250Å providing a ∼ 1.56Å/pix dispersion. This results in a spectral resolution that varies from R∼1000 (blue) to R∼1600 (red). This spectral resolution and wavelength range was selected to enable detection of at least the [OII] (3727Å) emission line and 4000Å break over our full target redshift range and provide sufficient velocity resolution with which to identify close pairs (<50 km sec^{-1}, see Robotham et al. 2014; Fuenblackba-Fuentes et al. 2025).

Spectroscopic observations for DEVILS were taken over ∼ 100 nights between December 2017 and January 2021, covering 25 separate observing runs. Observations were taken both in person at Siding Spring and remotely from a number of locations. We note here that the survey was originally planned to complete in 2020, but was significantly delayed due to a number of instrument/facility failures at the AAT and COVID-19 closures. Details of the DEVILS observational setup and measurements are also described in Section 5 of Davies et al. (2018), so we only briefly summarise key points here:

• **Calibrations sources:** Sky fibres are selected using blank sky positions taken from the ProFound segmentation maps, and each observation 25 blank sky positions were targeted. Flux standards were selected from SDSS using fibermag_r > 16.9 and 16.6 < psfmag_r < 18.4, and classified as either SPECTROPHOTO_STD or REDDEN_STD. We observe three spectroscopic standards in each observation. Finally, for guide stars we select all sources at 13.7<R1Mag<14.4 from the USNO-B guide-star catalogue and exclude sources with proper motions of >15 mas yr^{-1}, using 7-8 in each pointing.

• **Tiling and Fibre Assignment:** Priorities are assigned to targets based on their Y-band magnitude, with fainter sources having higher priority (to allow sources which will require longer integration times to be preferentially observed). Targets are assigned to fibres using the greedy tiling algorithm outlined in Robotham et al. (2010) and used in GAMA, which adds additional weights to priorities based on close on-sky clustering to allow complex regions with high levels of potential fibre collisions to be preferentially targeted.

• **Nightly Observations:** Fibre flat observations were taken with the Quartz_75_A, 75W lamp and arc observations with the FeAr_1, FeAr_2, CuAr_1, CuAr_2, CuHe_1, CuNe_1 lamps. Data are typically observed in a 6 sec flat, 45 sec arc, 2×1800 sec sequence. ∼ 30 dark frames are taken each run and 10 bias frames are observed each day.

• **Redshift feedback:** As discussed in Davies et al. (2018), within the DEVILS survey we use a 'redshift feedback' methodology to allow increased survey efficiency when simply aiming to maximise redshift completeness in a given sample. Briefly, in this mode we do not use fixed total integration times based on prior information regarding each source, but instead observe all targets for short ∼1h integrations. Following each new observation, we stack all data from a given source, and attempt to measure the source redshift. If a secure redshift is obtained we flag the source as complete and do not re-observe. If no secure redshift is obtained, we prioritise the source for re-observation the following night. In this manner sources are only observed for the minimum (rounded up to the nearest hour) exposure time required to obtain a secure redshift. Note that this process is also proposed for a number of the 4m Multi-Object Spectrograph Telescope (4MOST, de Jong et al. 2014) consortium surveys. For further details and motivation of this approach, see Section 6.2 of Davies et al. (2018) and Section 4.4.

4 NIGHTLY DATA REDUCTION AND ANALYSIS

Data reduction is primarily undertaken using the DEVILS observing preparation, data reduction and analysis pipeline (Tool for Analysis and Redshifting, TAZ). Given the redshift feedback mode described above, observations during the DEVILS survey must be reduced, combined with existing data, redshifts measured and tiling catalogues updated on a nightly basis. To undertake this, following nightly observations, all data and calibration files are synced to the DEVILS data processing machines. This triggers the automatic pipeline, which then runs the following broad steps.

4.1 Raw data reduction

The raw data were reduced using the AAO's 2DFDR software (Croom, Saunders, & Heald 2004) developed continuously since the advent of the 2dF and optimised for AAOmega. The software is described extensively in a number of AAO documents, so we do not cover it in detail here. Briefly, it performs automated spectral trace (tramline) detection, sky subtraction, wavelength calibration, stacking and splicing. As part of the automated 2DFDR reduction process, the blue and red spectra are flux calibrated to a white dwarf spectrum but with an arbitrary normalisation.

4.2 Data Combination

Following the raw data reduction, 1D target spectra from an individual night are extracted from the reduced data and stored in the DEVILS database. The database is then searched for all existing 1D spectra for a given target. All spectra for a specific target are then stacked in heliocentric-corrected wavelength space using an inverse variance weighting scheme. All individual 1D spectra are retained and the combined total stacked spectrum flagged as the current 'best' observations for a given source. All meta data on provenance, total exposure times, etc are retained with the stacked spectrum and included in the DEVILS targeting catalogues. An example of this process is shown for a single source in Figure 3. Moving from top to bottom we show successive stacks of source UID=101501853032307936 consisting of 4 ∼1h exposures over a period of 8 days in December 2017. We find that the signal-to-noise ratio (measured as a median SNR/pixel between 6500-7000Å) increases by $\sim 1/\sqrt{T_{exp}}$ with successive exposures, as expected.

4.3 Rough Flux calibration

Following this, we perform our own additional arm-specific flux calibration on the stacked spectra using the DEVILS broad-band photometric data. For this we use the HSC-g (blue arm) and HSC-i (red arm) photometric filters to measure the spectral flux in each band. We then re-calibrate the AAOmega spectra to have the same spectro-photometric flux as the photometry catalogues and then re-combine spectral arms into a full spliced spectrum. We note that this process is not highly accurate, however flux calibrated spectra are not required for any of the core DEVILS science goals.

4.4 Redshift Measurements

With reduced, calibrated and stacked spectra in hand, we now undertake automatic redshifting on all 'best' stacked spectra for each newly-observed target. This is performed using an adapted version of the AutoZ redshifting code (Baldry et al. 2014). Full details of this process and its effectiveness in obtaining redshifts from AAOmega

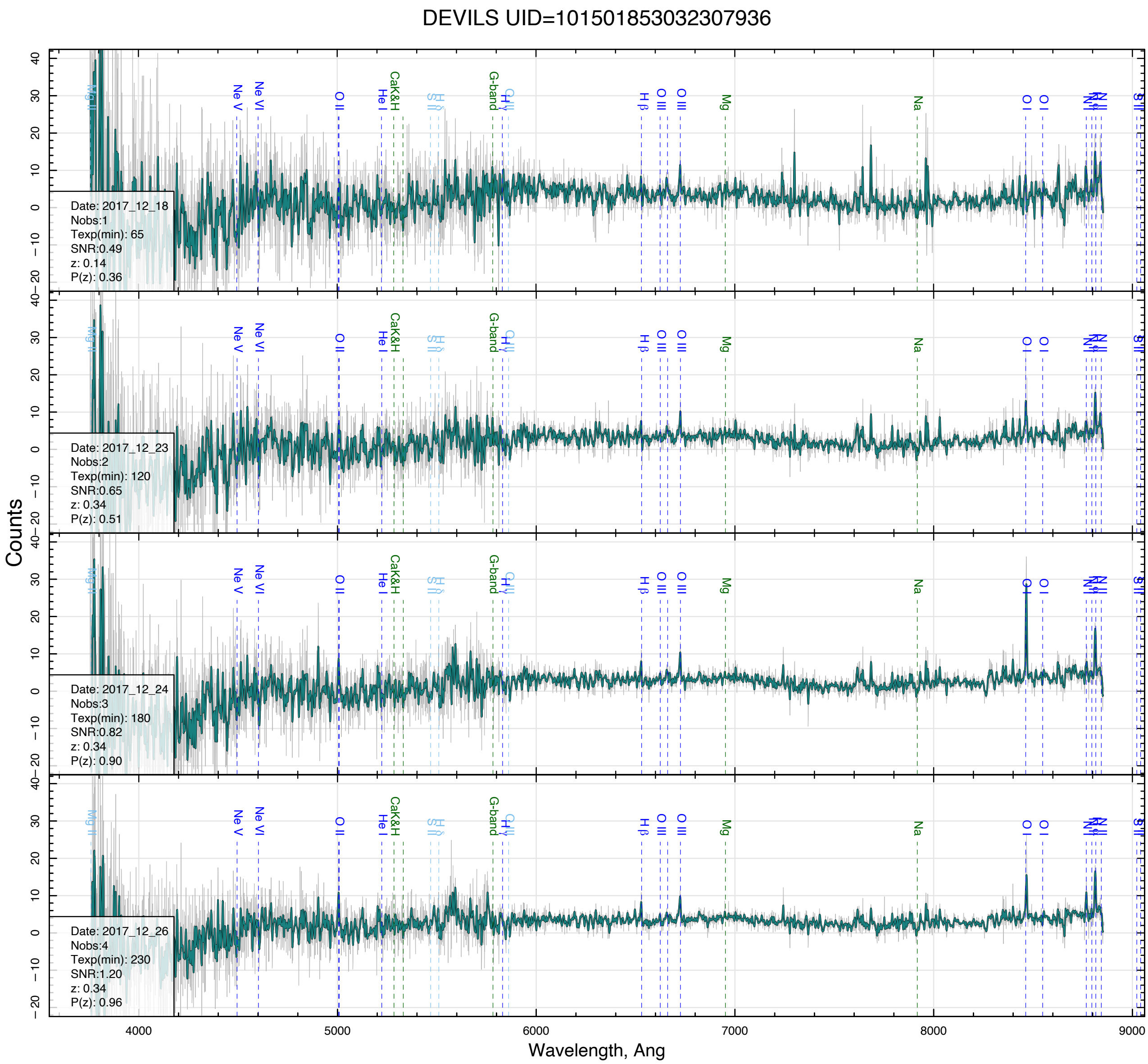

Figure 3. Examples of 1D DEVILS spectra for source UID=101501853032307936 indicating the DEVILS inverse variance-weighted stacking procedure. Faint grey lines show the raw AAOmega spectrum, solid green lines show a Hanning smoothed version of this spectrum. Key emission (blue), absorption (green) and AGN (light blue) lines at the final source redshift are shown as vertical dashed lines. Panels from top to bottom show successive stacks of data building up exposure time and increasing signal-to-noise. The last observation date, number of observations, total exposure time, SNR (measured as a median SNR/pixel between 6500-7000Å), best-fit redshift and redshift probability, P(z), are given in the legend. In the top panel the source is too low signal-to-noise for the correct redshift to be obtained. In the second/third panels the correct redshift is found, but the P(z) is too low for this to be secure. In the bottom row, the correct redshift is found at a high probability and the source stops being observed.

spectra using an almost identical set-up to that used in DEVILS are described in the aforementioned work. The AutoZ code not only provides galaxy redshifts but also a probability that the redshift is correct, P(z) - see Baldry et al. (2014) for details. We note here that in this analysis we retain the top 5 redshift solutions and probabilities for each source.

Within the DEVILS observations we initially assign a P(z)>0.95 as a secure redshift. During the nightly redshifting process, objects that obtain a redshift with P(z)>0.95 are flagged as having a secure redshift and their targeting probability is set to P0 (do not target). Objects which have been observed, but do not have a secure redshift are set to P7 (highest priority). This ensures that an object which has started to be observed, is highly likely to be re-observed in subsequent observations, such that observation time is not wasted. We also enforce the maximum exposure time, T_{max}, for all sources. This ensures that objects do not continue to receive further exposures if they will likely not obtain a redshift with a 4m-class facility. We set T_{max} =15h. Objects which reach a total exposure time of >15h but a P(z)<0.95 are also set to P0. The redshift feedback process is also displayed in the successive spectra in Figure 3. Here we see that after the first exposure the P(z) value is low and the redshift is incorrect compared to the final solution. After the second exposure the correct redshift was obtained but the P(z) is low, so the object is re-observed. After the third exposure the same redshift is obtained, with a higher P(z), but not above our P(z)>0.95, defined for a secure redshift. After the fourth exposure P(z)>0.95, the redshift is deemed secure and we stop observing this source for the remainder of the survey.

4.5 Tiling catalogue updates

Once redshifting is complete and new targeting probabilities are assigned, the final stage of the pipeline is to produce new 2dF target fibre assignments and observing catalogues following the process outlined in Section 3. These are then returned to the observers at the telescope ready for the next night's observations.

The process of running the pipeline typically takes a few hours, such that nightly datasets can be reduced and updated target catalogues returned to the observatory in time for the following night's observations. We also note that following the completion of the survey a full reduction of the entire sample was undertaken with slightly modified settings to improve the data reduction. The final DR1 contains data produced by this final re-reduction/analysis which aims to maximise the redshift recovery rate. In Figure 4 we show a number of random examples of the final-reduced DEVILS spectra, with redshift assignments overlaid.

5 SAMPLE DIAGNOSTICS

In the following section we detail a number diagnostics of the final DEVILS DR1 dataset. We note here that our final DEVILS D10 sample contains unique observations of 10,159 sources covering a range of exposure times, over a total of 40,375 fibre-hours of AAT observing time, with a median of 4h exposure time per source. From this sample we initially obtained 5,442 redshifts with a P(z)>0.95. In Figure 5 we show the redshift accumulation rate as a function of time, highlighting the observability epochs of the D10 region in grey. Redshifts accumulate rapidly in the observable windows. The exception to this is the 2020 observing block, which was impacted by COVID closures and instrument failures. In Figure 6 we then show the resultant distribution of P(z) values as a function of signal-to-noise (measured as a median signal-to-noise per pixel between 6500-7000Å). All objects remain at a relatively low signal-to-noise as we stop observing sources once they reach a P(z)>0.95. As such, sources in this figure that have P(z)<0.95 are those that we did not obtain a secure redshift over the duration of the survey. In figure 6 we then also match our DEVILS sources to those with secure redshifts from the COSMOS spectroscopic redshift catalogue of Khostovan et al. (2025). There are 3,936 sources from the COSMOS catalogue that were observed in DEVILS (without filtering on P(z)). We identify sources which have the consistent redshift based off the offset between redshift measurements as:

$$\frac{|(z_{\rm COSMOS} - z_{\rm DEVILS})|}{(1 + z_{\rm DEVILS})} < 0.15 \quad (1)$$

We find that 3,012 sources have consistent redshift between DEVILS and COSMOS, and of the remaining 924 sources, ~90% (826) have a P(z)<0.95. *i.e.* for a comparison to the COSMOS catalogue only 98 sources have a P(z)>0.95 and a redshift which differs between the two samples. We visually inspect all of these sources and compare to the COSMOS2015 photometric redshifts of Laigle et al. (2016), and find that the reasons for these discrepancies are varied. We find source where the DEVILS redshift appears correct and aligns with the photometric redshift (but differs from the COSMOS spectroscopic redshift), objects where stars are misidentified as galaxies and vice versa, objects where poor sky subtraction has led to line misidentification and objects which show clear AGN-like spectra (which are not accounted for in our redshift measurements with AutoZ). Given the small fraction of objects, we do not aim to manually fix these in our initial DEVILS redshifts. However, in Section 6 when we build our master redshift catalogue, we weight our final redshifts based on a combination of available redshifts for each target, and note that the majority of these cases are updated in this approach - leading to greater consistency between our final redshifts and the COSMOS spectroscopic catalogue.

5.1 ExposureTimes for Faint Sources

Given the nature of DEVILS, which aims to provide a deep but high-completeness spectroscopic sample of galaxies at intermediate redshifts, it is interesting to explore the observational difficulties with obtaining redshifts at these magnitudes/epochs. This not only describes one of the core diagnostics for the resultant DEVILS sample, but also provides key information required for the planning and execution of future deep redshift surveys, such as 4MOST-WAVESdeep which will target similar populations to DEVILS. As described in Section 4.4, one of the biggest complications with this process is our inability to define the required exposure time to obtain a redshift for faint sources. To highlight this, Figure 7 shows the final total exposure times required to obtain a secure redshift, as a function of r-band magnitude. In the left panel we highlight the running median and interquartile range of exposure times for a secure redshifts. We also over-plot the ~r-band limits of the SDSS, GAMA and WAVES spectroscopic samples. Clearly we see here that for surveys such as SDSS and GAMA, little is gained from going beyond fixed short exposure times. However, as we move to fainter galaxies, the exposure time required to obtain a redshift can vary highly, such that using fixed exposure times is no longer practical. As such, exposure times are problematic to estimate a priori and using a redshift-feedback methodology significantly improves survey efficiency. A potential solution to this is to use colour information to better predict required exposure times. However, as shown, in the right panel of Figure 7, these exposure times are not significantly different for red and blue populations (in the observed frame), such that this information largely does not help in a priori predicting exposure times for faint sources - further motivating the redshift feedback methodology.

5.2 Comparison to existing redshifts

Next we further compare our DEVILS-AAT redshifts to existing known redshifts in the DEVILS-D10/COSMOS region. There are a large number of redshift campaigns in COSMOS. These will be used to build our master redshift catalogue and will be described extensively in Section 6. Here we simply show a comparison to a number of key programs in order to validate the redshift measurements obtained from our DEVILS AAT spectra.

First, for an initial visual comparison we identify sources that have a common observation across multiple surveys where 1D spectra are publicly available. In our DR1 data release we ultimately provide matched and standardised DEVILS-AAT, zCOSMOS, and DESI EDR 1D spectra for our D10 targets. As such, for initial visual comparison we identify 171 sources which have an observation, and secure redshifts, in all of DEVILS-AAT, zCOSMOS and DESI. This number is small, as we deliberately do not target the majority of

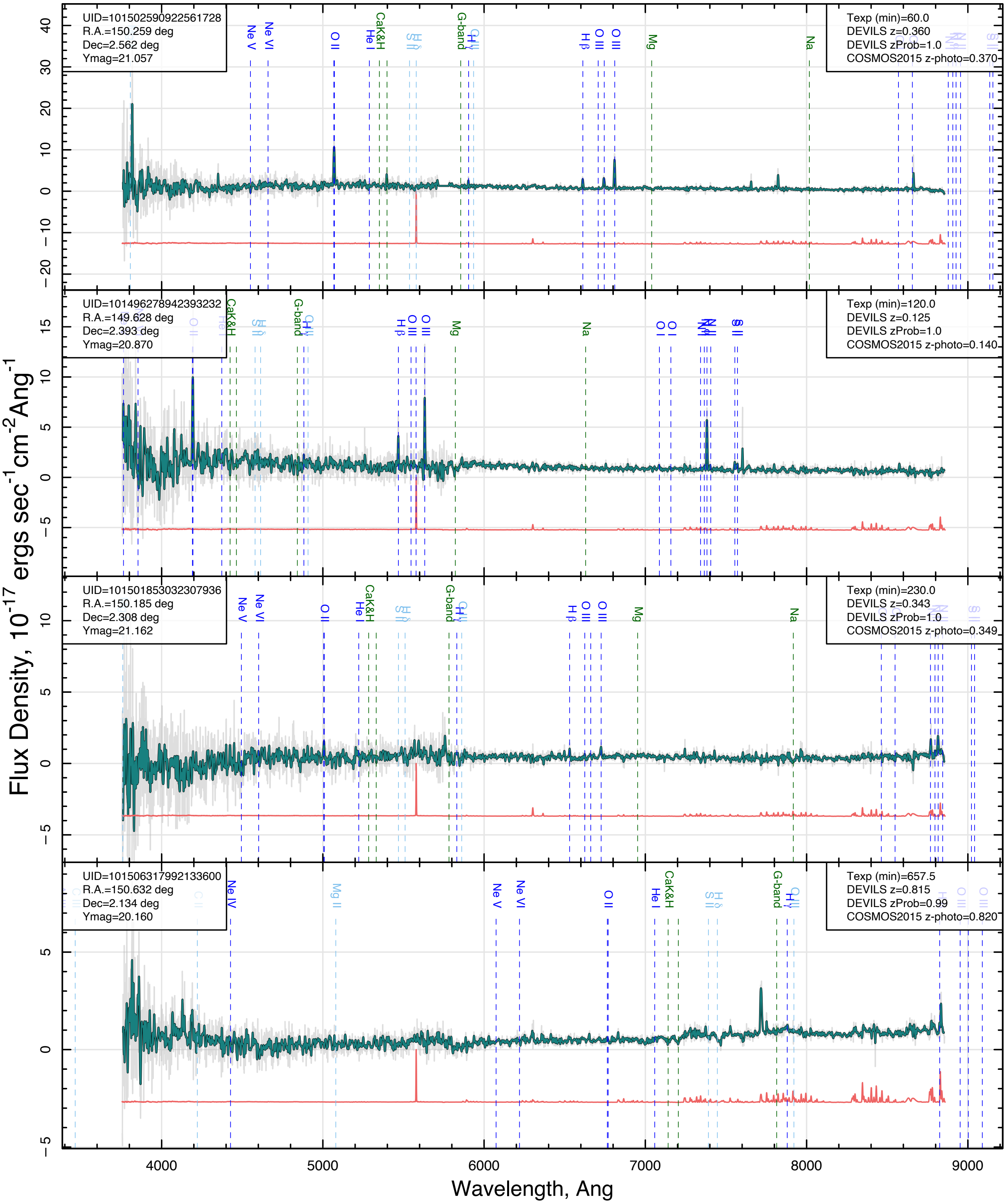

Figure 4. Examples of 1D DEVILS spectra from our final reduced sample. Here we show random examples for faint sources at a range of redshift and requiring a range of exposure times to obtain a secure redshift (given in the top left legend). Faint grey lines show the raw AAOmega spectrum, solid green lines show a Hanning smoothed version of this spectrum, red lines show the sky spectrum offset for clarity. Key emission (blue), absorption (green) and AGN (light blue) lines at the source's redshift are shown as vertical dashed lines.

Table 1. Surveys used to compile redshifts in our `devils_dr1.D10MasterRedshifts` catalogue. [1] Number of sources with any redshift measurement in the D10 region. [2] filter used to define a robust redshift for this survey. [3] Number of sources used as `zBest` in the final `devils_dr1.D10MasterRedshifts` catalogue. Objects are assigned `zBest` in order of priority from top to bottom in the table with the filter column applied. [4] Median VISTA Y-band AB magnitude of `zBest` objects from this sample. [5] Notes on sample containing the method used to measure redshifts and the probability measure given in the `devils_dr1.D10MasterRedshifts` catalogue. Redshifting approaches: AutoZ=Automatic redshift code (Baldry et al. 2014), EZ=Easy Redshift (Garilli et al. 2010), cross-corr= cross-correlation between templates and galaxy spectra, SpecPro= Interactive tool for visual classification (Masters & Capak 2011), Visual = visual inspection of galaxy redshifts, EAZY=photometric redshift fitting code (Brammer, van Dokkum, & Coppi 2008), Le Phare=photometric redshift fitting code (Arnouts & Ilbert 2011). Probability types: P(z)=correct redshift probability, flag=numeric flag assigned to redshift quality (can be different for different surveys, but DR1 documentation describes flag meanings for each survey), correlation=strength of the cross-correlation peak between the best-fit template and galaxy spectrum.

Name	Type	Facility	#[1]	z_{med}	filter[2]	# zBest[3]	Y_{med}[4]	Ref.	Note[5]
DEVILS	Spec	AAT-AAOmega	10,005	0.47	DEVILS_probPlus>0.95 OR DEVILS_probPlus>0.90 if zBestType!=‘spec’	7,946	20.46	This work	AutoZ redshifts, prob=P(z)
zCOSMOS	Spec	VLT-VIMOS	18,957	0.56	3≤zCOSMOS_prob<5 OR 13≤zCOSMOS_prob<15 OR 23≤zCOSMOS_prob<25	10,940	20.76	Lilly et al. (2007)	EZ redshifts, prob=flag
DESI	Spec	Mayall-DESI	10,206	0.73	DESI_prob≥9 & ZWARN==0	6,428	21.71	DESI Collaboration et al. (2024)	RedRock, prob=DELTACHI
hCOSMOS	Spec	MMT-Hectospec	4,208	0.32	None	754	19.67	Damjanov et al. (2018)	cross-corr, prob=correlation
LEGA_C	Spec	VLT-VIMOS	1,880	0.76	None	679	21.44	van der Wel et al. (2016)	cross-corr, prob=correlation
VVDS	Spec	VLT-VIMOS	4	0.69	VUDS_prob=1.5,2,3,4,>10	1	22.18	Le Fèvre et al. (2013)	EZ, prob=flag
VUDS	Spec	VLT-VIMOS	156	2.51	3≤VVDS_prob≤5	148	24.13	Le Fèvre et al. (2015)	EZ, prob=flag
FMOS	Spec	Subaru-FMOS	1,150	1.56	3≤FMOS_prob≤5	288	22.64	Silverman et al. (2015)	SpecPro, prob=flag
MOSDEF	Spec	Keck-MOSFIRE	564	2.29	MOSDEF_prob≥4	357	24.01	Kriek et al. (2015)	Visual, prob=flag
C3R2	Spec	Keck-Multi	2,622	0.86	3≤C3R2_prob≤4	2,238	22.97	Masters et al. (2019)	Visual, prob=flag
DEIMOS	Spec	Keck-DEIMOS	7,440	0.89	DEIMOS_prob=2 OR 1.5	4,739	22.41	Hasinger et al. (2018)	SpecPro, prob=flag
LRIS	Spec	Keck-LRIS	433	2.50	3≤LRIS_prob≤4	234	23.74	Lee et al. (2018)	Visual, prob=flag
ComparatOII	Spec	VLT-FORS2	1,440	1.14	None	657	22.11	Comparat et al. (2015)	Visual, prob=flag
VIS3COSMOS	Spec	VLT-VIMOS	653	0.84	None	354	22.11	Paulino-Afonso et al. (2018)	SpecPro, prob=flag
PRIMUS	Grism	Baade-IMACS	27,466	0.57	None	5,590	22.06	Cool et al. (2013)	Grism+photometry cross-corr
3DHST	Grism	HST-G141	3,797	0.94	None	1,463	23.19	Momcheva et al. (2016)	Grism+photometry EAZY
PAU	Photo	WHT-PAUCam	37,474	0.64	None	13,885	22.03	Alarcon et al. (2021)	40 Narrow-band SED-fits
COSMOS2015	Photo	Multi	507,395	1.15	None	451,276	24.71	Laigle et al. (2016)	Le Phare
MIGHTEEtmp	Photo	Multi	494,179	1.13	None	221,980	26.09	Adams et al. (2020)	MIGHTEE team Le Phare

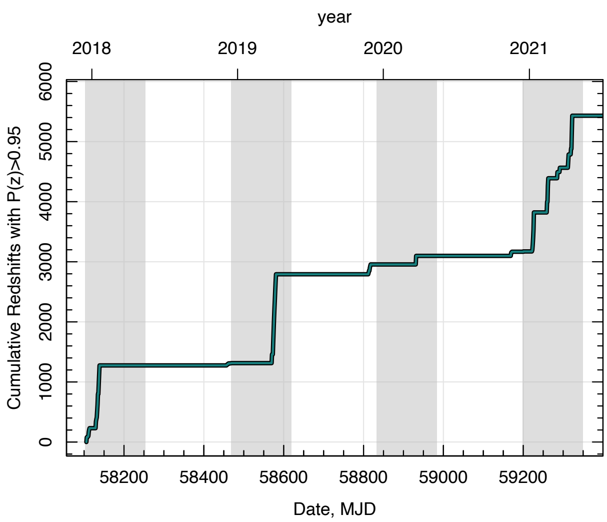

Figure 5. Secure, P(z)>0.95, redshift accumulation rate in the D10 as a function of time. Grey shaded region shows the period when the D10 field was observable from the AAT for >4h/night. The 2020 observing block was significantly affected by COVID shutdowns and instrument failures.

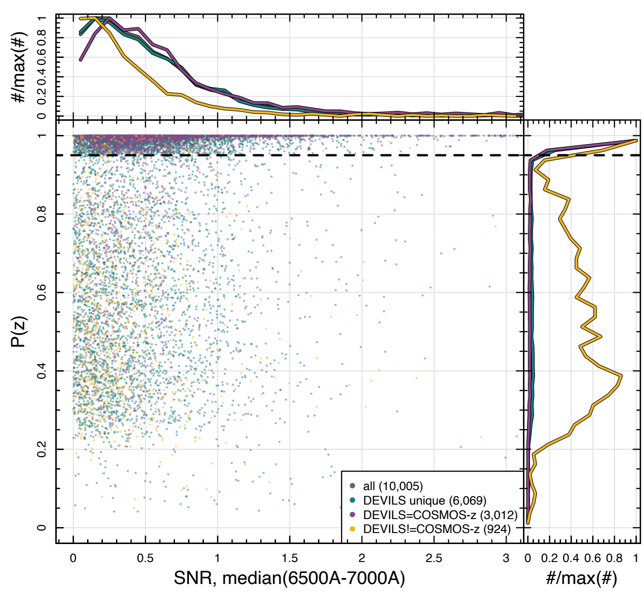

Figure 6. Redshift probability measurement, P(z), as a function of signal-to-noise ratio. Here we also compare DEVILS measurements with those taken from the COSMOS spectroscopic redshift compilation. Green points/lines show sources with unique DEVILS AAT redshifts, purple points/lines show sources which have the same redshift as in the COSMOS spectroscopic redshift compilation, while gold points/lines show sources where our DEVILS-AAT redshifts differ from the COSMOS spectroscopic redshift compilation. The majority of these sit at low P(z) values. The dashed horizontal line shows P(z)>0.95.

zCOSMOS objects with our DEVILS-AAT observations - but provides a direct comparison point for the three surveys. We visually inspect these spectra and find 97.5% agreement between DESI EDR and DEVILS-AAT redshifts and 95.2% agreement between zCOSMOS and DEVILS-AAT - and also note that the small number of sources which disagree on redshifts are different between DESI EDR and zCOSMOS (96.8%). An example of this visual comparison, se-

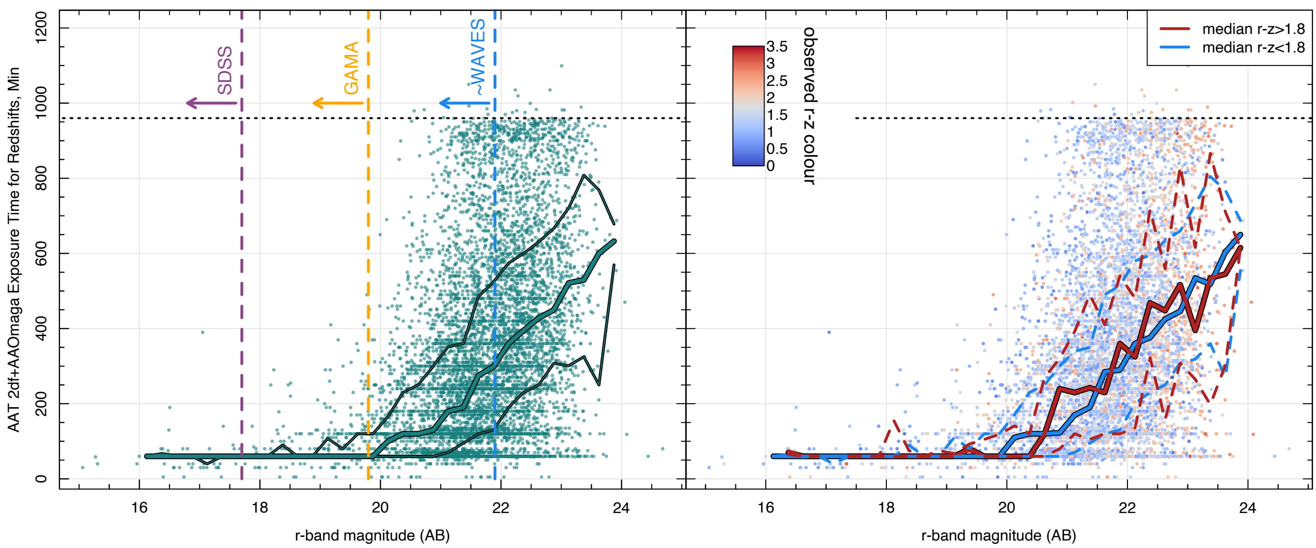

Figure 7. Exposure times required to obtain a secure spectroscopic redshift from our DEVILS AAT+AAOmega data as a function of r-band magnitude. The left panel shows all sources, with the green lines displaying the running median and interquartile range. We also over-plot the spectroscopic target limits SDSS (purple), GAMA (orange) and upcoming WAVES (blue). The right panel shows the same but colour-coded by observed-frame $r - Z$ colour. These running median's show very little difference between red and blue populations, suggesting at these faint magnitudes observed-frame colour is not a strong predictor of the exposure time required to obtain a redshift. A redshift-feedback methodology (as described in the text) overcomes all of these issues, by having no fixed exposure time and also not relying on a priori information to determine an exposure time.

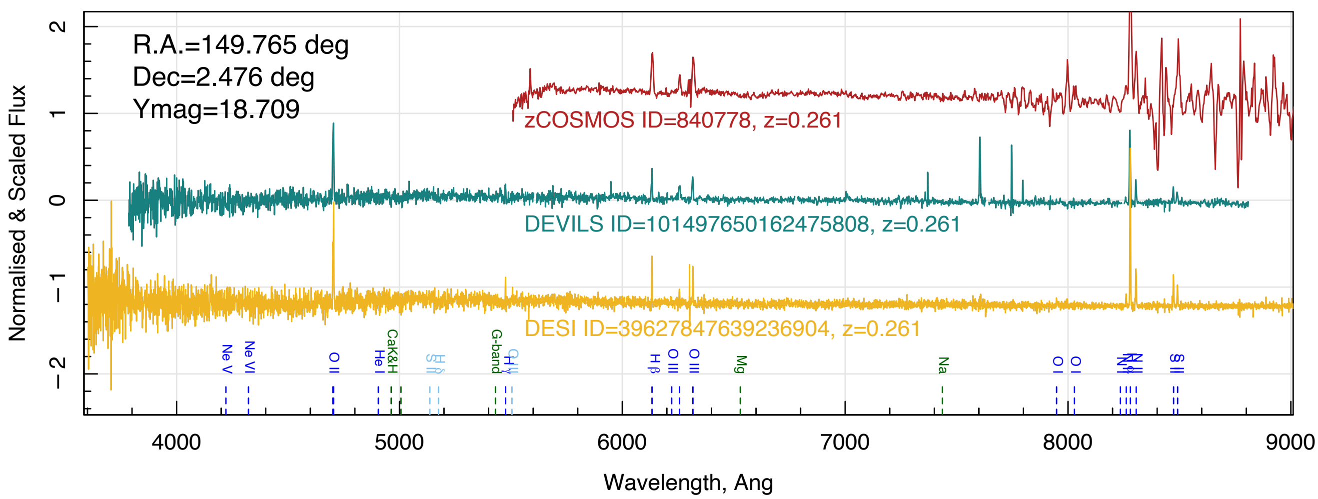

Figure 8. Example DEVILS AAT spectrum (green) for source UID=101497650162475808 for which both zCOSMOS (red) and DESI (gold) spectra are also available. Spectra are scaled to the same noise level and normalised to offset flux values for clarity. All surveys obtain the same redshift assignment for this source.

lected where all redshifts agree, is shown in Figure 8 for a single source.

Next, we take DEVILS galaxies with P(z)>0.95 and perform a 2 arcsec positional match to the COSMOS spectroscopic redshift compilation of Khostovan et al. (2025). We note that this sample also contains redshifts from the DESI EDR and zCOSMOS as noted above. In the top panel of Figure 9 we show a comparison of redshift measurements for this matched sample, reiterating the agreement discussed perviously. Next in Figure 9 we show comparisons to robust (Q=3-4) grism redshift from the PRIsm MUlti-object Survey (PRIMUS, Cool et al. 2013), highly-precise narrow-band photometric redshifts from the Physics of the Accelerated Universe Survey using PAUCam (PAUS, Alarcon et al. 2021) and COSMOS2015 photometric from Laigle et al. (2016). These redshifts are matched to DEVILS-AAT sources using the methodology outlined in Section 6 (using the DEVILS segmentation maps). In the top right legend in Figure 9 we note the number of sources matched between each sample, the mean absolute deviation (MAD) of the redshift offsets and outlier fraction, with outliers defined as sources with $|(z_X - z_{\rm DEVILS})/(1+z_{DEVILS})| > 0.15$ (where X is the survey being

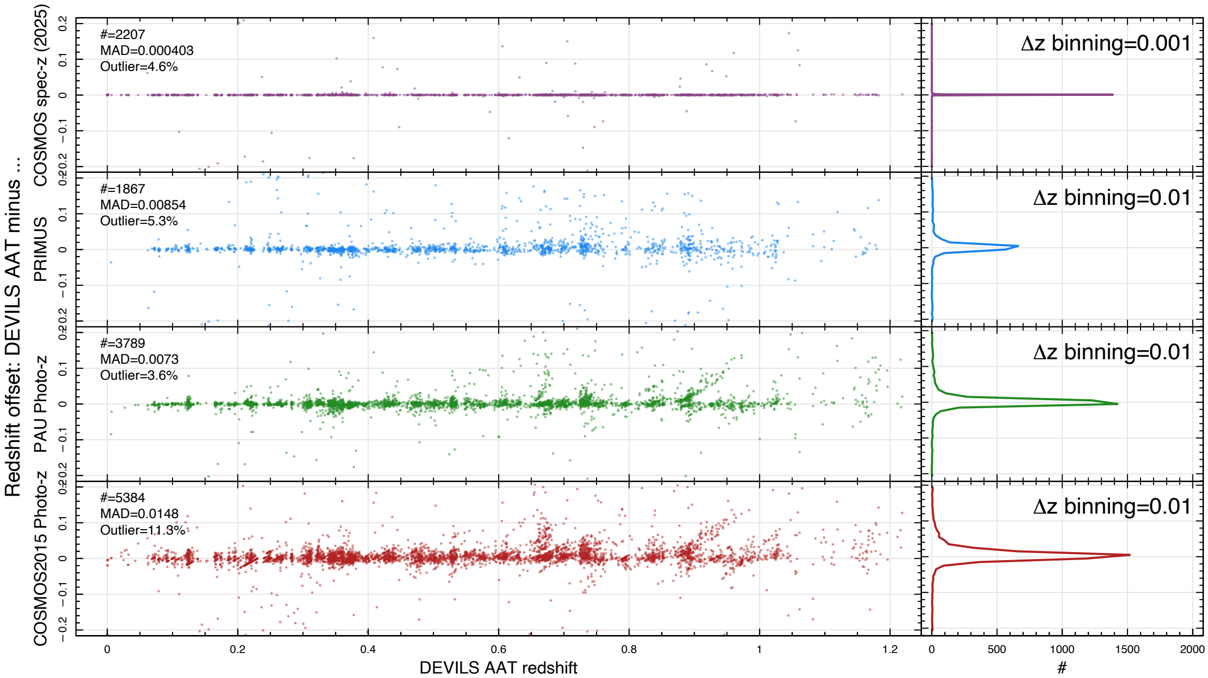

Figure 9. Comparison between our DEVILS-AAT spectroscopic redshifts and other redshift measurements for the same sources. The left panels show Δz of DEVILS-AAT - X as a function of the DEVILS-AAT redshifts. The number of sources in the comparison, mean absolute deviation (MAD) and outlier fraction are given in the top left. Outlier fraction is defined as $|(z_X - z_{\rm DEVILS})/(1 + z_{DEVILS})| > 0.15$ .The right panels show a histogram of Δz values. Note, binning for Δz histograms is finer for the spectroscopic comparison in the top row to show the tighter relation - binning is noted as ΔzOffset. The top row shows a comparison with the recent COSMOS spectroscopic complication of Khostovan et al. (2025) in purple, next row shows a comparison to PRIMUS grism redshifts in blue, next row shows a comparison to PAU photometric redshifts in green, and the bottom row shows a comparison to COSMOS2015 photometric redshifts.

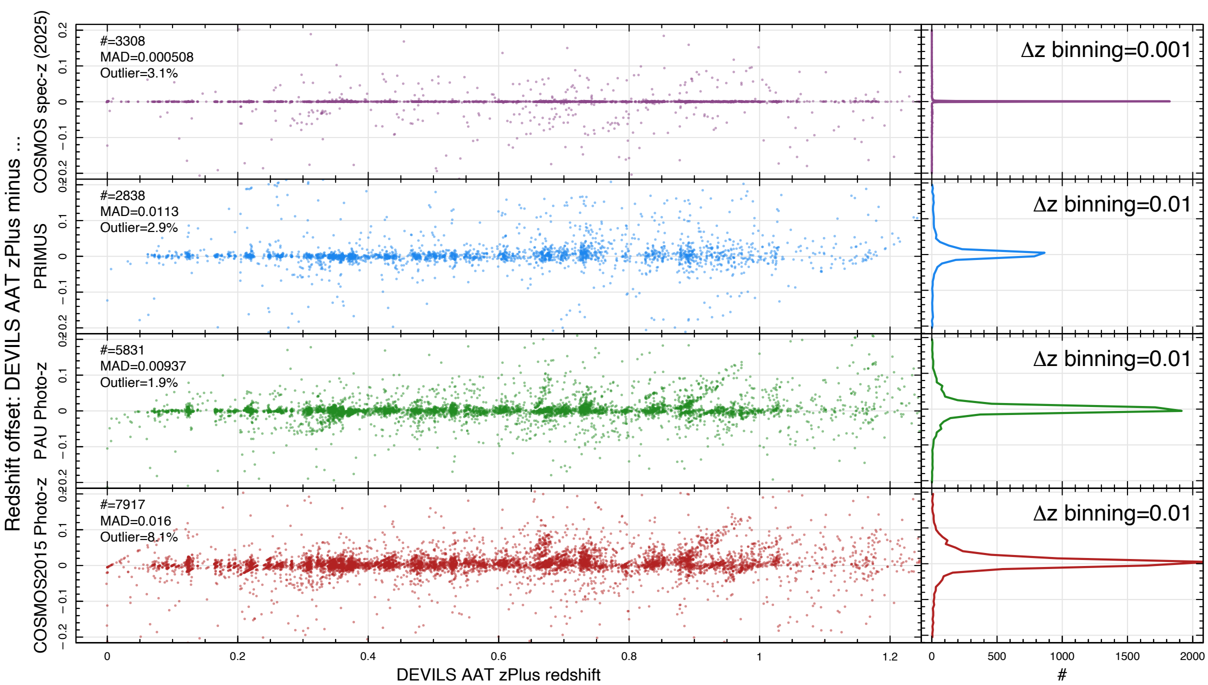

Figure 10. The same as Figure 9 but now showing comparisons to our `DEVILS_zPlus` redshifts (DEVILS-AAT redshifts weighted by other survey redshifts in the COMSOS region).

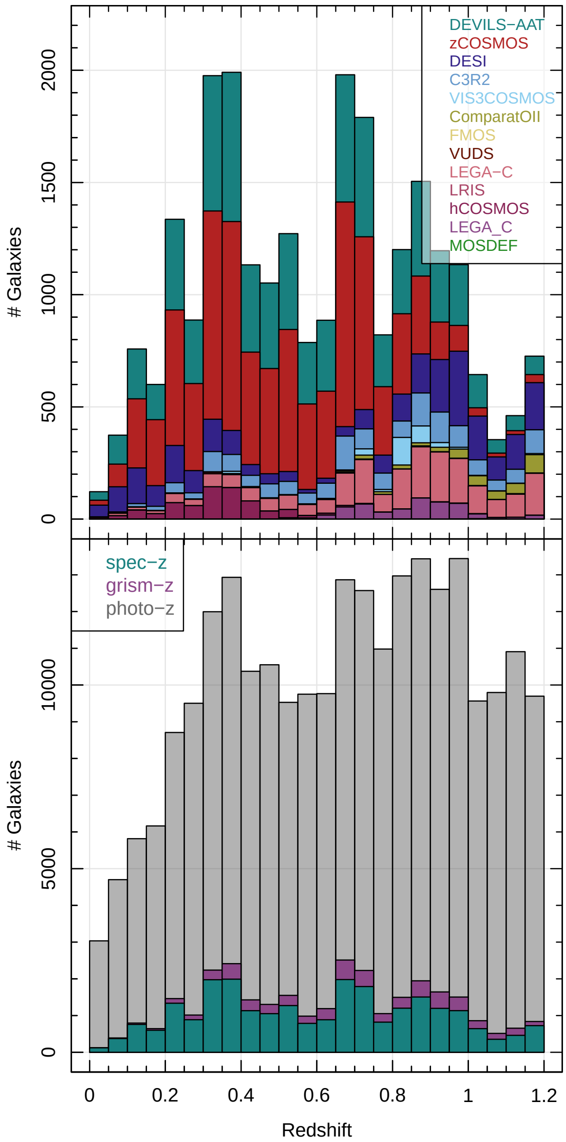

Figure 11. Redshift samples included in the `devils_dr1.D10MasterRedshifts` catalogue. Top panel shows the breakdown of `zBest` values for various spectroscopic samples over various campaigns (given as `zBestSource` in the catalogue), bottom panel shows a comparison of spectroscopic, grism and photometric redshifts (given as `zBestType` in the catalogue) going into the final `zBest` value. Both panels show the full distribution of sources over this redshift range, with no magnitude limit imposed.

compared to). All samples show good agreement with our DEVILS-AAT redshifts, with low outlier fraction and low MAD (see figure for details). As such, overall we find good agreement between our new DEVILS-AAT redshifts and those for other surveys in the D10 region. We see no systematic biases in our redshift assignments, which would bias any scientific analyses with this sample.

6 COMPILATION OF D10 REDSHIFT CATALOGUE

As noted previously, there are a large number of surveys that have measured redshifts in the D10 region. These range from relatively low precision/accuracy broad-band photometric redshifts, to high precision/accuracy spectroscopic redshifts. In order to build science-ready `devils_dr1.D10MasterRedshifts` catalogue, we combine all available redshifts for sources in the region. In this section we describe the origin of redshifts used in the `devils_dr1.D10MasterRedshifts` catalogue, how they are matched to sources in the DEVILS photometry catalogue (`devils_dr1.D10ProFoundPhotometry`), how we derive 'improved' DEVILS-AAT redshifts and probabilities using existing redshift information and finally how we assign a 'best' redshift to each source in the `devils_dr1.D10ProFoundPhotometry` catalogue.

First, in Table 1 we outline the various surveys used in our redshift compilation. Note this is an updated version of the compilation presented in Thorne et al. (2021). In the `devils_dr1.D10MasterRedshifts` catalogue we provide all individual redshift measures that are associated with a given source. The number of sources with redshifts provided by a particular sample and the median redshift is given in Table 1. In order to match redshifts for the same source, we utilise the ProFound segmentation maps derived in our photometric analyses discussed in detail in Davies et al. (2021). Briefly, these maps associate imaging pixels to a particular source in a deep NIR stacked image using UltraVISTA imaging. To match sources, we first identify all sources from a given redshift catalogue from Table 1 which lie within the segment of a particular DEVILS photometric source. If multiple sources from the same catalogue fall within a single DEVILS photometric source, we take the closest object to the flux-weighted centre of the segment. The matched source redshift values are then attached to this DEVILS source, and added to the `devils_dr1.D10MasterRedshifts` catalogue.

6.1 Weighting based on redshift agreement

To this point, we have assigned the DEVILS-AAT redshifts in isolation. However, the additional redshift information for other surveys in the COSMOS region can help better constrain the correct galaxy redshifts from our AAT spectra. This is particularly true when including information from low precision measurements from *e.g.* photometric redshifts. For example, if a low P(z) redshift solution from our AutoZ analysis is consistent with the photometric redshift (or grism or existing spectroscopic redshift), this adds additional weight to that particular solution. As such, we can use the existing redshifts in the COSMOS region to further improve both our redshift assignment and probabilities. We do not apply this process in our initial analysis, as we wish to retain our direct AutoZ redshifts measured only from of DEVILS-AAT spectra, but add additional columns to the final `devils_dr1.D10MasterRedshifts` catalogue for these new redshifts and probabilities (hereafter, `DEVILS_zPlus` and `DEVILS_probPlus`).

To undertake this process, we return to our original AutoZ outputs containing the top 5 redshift solutions for each source. We then compare each of these solutions to the matched redshifts from all of the other surveys described above. First, we do not include the MIGHTEEtmp photometric redshifts in this analysis as the photometric redshift have low precision and are largely used to fill the faint sample where no COSMOS2015 photometric exists. For the COSMOS2015 photometric sample, we use the lower and upper 1σ bound to the photometric redshift P(z), provided in the COSMOS2015 catalogue, and check if any of our DEVILS AutoZ redshifts fall within this range. This is then deemed as a match. For all other surveys we use the metric for redshift agreement as:

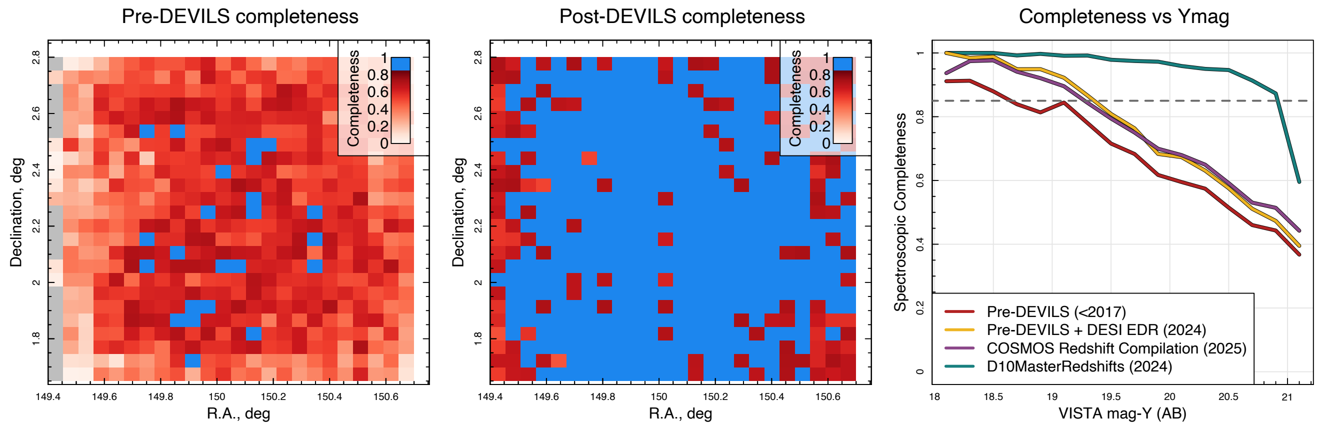

Figure 12. Left: The spatial completeness of DEVILS targets with pre-DEVILS robust spectroscopic redshifts. Middle: The spatial completeness of DEVILS targets with post-DEVILS robust spectroscopic redshifts. Grid cells with completeness > 85% are shown in blue. Right: The spectroscopic completeness as a function of Ymag for a pre-DEVILS sample, pre-DEVILS sample + DESI EDR redshifts, the recent COSMOS Spectroscopic Redshift Compilation Catalog and full DEVILS sample taken from the `devils_dr1.D10MasterRedshifts` catalogue. The dashed horizontal line shows a completeness of 85%, which is required for high completeness science (*e.g.* group finding). The DEVILS sample extends to roughly 1.5 magnitudes fainter than other samples at this completeness.

$$|ln(1+z_{\rm DEVILS}) - ln(1+z_X)| < lim_{\rm type}$$

where z_X is the redshift from the survey in question, and $lim_{\rm type}$ is a variable limit depending on the redshift type (spec, grism, photo) where: $lim_{\rm spec}$=0.005, $lim_{\rm grism}$=0.025, and $lim_{\rm photo}$=0.05. We initially define the new `DEVILS_probPlus` variable equal to the raw AutoZ P(z) values for that solution. We then apply the following additions to this value:

• If the DEVILS AutoZ redshift aligns with any existing photometric redshift, `DEVILS_probPlus` = `DEVILS_probPlus`+1

• If the DEVILS AutoZ redshift aligns with any existing grism redshift, `DEVILS_probPlus` = `DEVILS_probPlus`+2

• If the DEVILS AutoZ redshift aligns with any existing spectroscopic redshift, `DEVILS_probPlus` = `DEVILS_probPlus`+4

In this process, any source with a `DEVILS_probPlus`>1.0 delineates that multiple redshift sources agree, and the decimal values indicate the original AutoZ P(z). All of these are also additive, such that a source with a DEVILS AutoZ redshift that aligns with a photometric, grism and spectroscopic redshift will have a value of `DEVILS_probPlus`=7.xx. We then determine the new best DEVILS AutoZ redshift based on the highest `DEVILS_probPlus` value and assign this as `DEVILS_zPlus`.

We find that through this process, 2,539 sources are added as having a robust redshift. Of these, 1,432 DEVILS sources change their initial redshift assignment (*i.e.* `DEVILS_z!=DEVILS_zPlus`), the rest simply have their initial redshift up-weighted in probability. Of the sources that change redshift, only 217 were initially assigned a P(z)>0.95 - such that we are largely just adding to the sample from low confidence redshifts which now have an up-weighted probability based of existing redshift information. Of the sources where the redshift is changed, 845 have a redshift consistent with an existing photometric redshift, 488 are consistent with an existing grism redshift and 372 are consistent with an existing spectroscopic redshift.

In Figure 10 we show the same as Figure 9, but now using our new `DEVILS_zPlus` redshifts. We find the number of robust redshift matches between samples goes up considerably, and outlier fractions are reduced for all comparisons.

Once sources are matched we then aim to identify the 'best' redshift available for a particular photometric source (hereafter `zBest`). To do this will apply an order of priority from bottom to top in Table 1, with the filters applied. For example, sources are initially assigned a MIGHTEEtmp photometric redshift, then if a COSMOS2015 redshift exists, `zBest` is updated, next if a PAU redshift exists, `zBest` is updated, and so on. Note that for this process we now use the `DEVILS_zPlus` and `DEVILS_probPlus` values over the initial DEVILS redshifts. Quality filters are applied to the spectroscopic catalogues as to ensure a robust redshift is used. These filters are provided in Table 1 and notes on the *_prob value in these filters are given in the final column (*i.e.* zCOSMOS provides a quality flag, while DESI provides a Δchi^2 value). In our final catalogue we provide all of these values. Once the filters are applied and `zBest` obtained, the number of sources from each sample used in this `zBest` are given in the table, along with the median Y-mag for the sources used. In Figure 11 we show the resultant distribution of `zBest` values. The bottom panels show the breakdown between spectroscopic, grism and photometric redshifts, while the top panel shows the breakdown from individual spectroscopic samples.

6.2 Completeness

Using the `zBest` values obtained above, it is interesting to consider how our final spectroscopic redshift sample compares to existing samples. In Figure 12 we show the pre-DEVILS spatial spectroscopic redshift completeness to Ymag< 21.2 DEVILS targets (left) and the final spatial spectroscopic redshift completeness using the `zBest` values defined above. In the right panel of Figure 12 we show this completeness as a function of Ymag. Here we show the DEVILS `devils_dr1.D10MasterRedshifts` completeness in green, the pre-DEVILS completeness in red, the pre-DEVILS + DESI EDR completeness in gold and the completeness from the COSMOS spectroscopic redshift compilation of Khostovan et al. (2025) in purple.

DEVILS obtains a spectroscopic redshift completeness of > 85% to ∼1.5 magnitudes fainter than other samples - achieving our goal.

To highlight the benefit of this high completeness, in Figure 13 we then show the light-cone distribution of galaxies in the D10 region at $0.5<z<0.6$. Here points are coloured by their stellar mass taken from the `devils_dr1.D10ProSpectAGN` catalogue described in the following section. On the left, we show the distribution of objects assuming a GAMA-like selection (*i.e.* high spectral redshift completeness in the local Universe), which can not map any large-scale-structure at these redshifts. In the middle-left we show the pre-DEVILS sample, where the large-scale-structure can be seen, but individual structures contain a smaller number of objects and faint filaments are hard to discern. On the middle-right we show the resultant sample from the `devils_dr1.D10MasterRedshifts` catalogue where individual structures contain a larger number of objects (allowing more robust measurements of halo mass, etc) and faint filaments are visible out to z=0.6. On the right we show new objects added by the DEVILS observations, which trace the same large-scale-structure. Interestingly, DEVILS predominantly adds higher stellar mass galaxies, which are typically passive and have therefore been missed by existing surveys.

Finally, we then explore the stellar-mass completeness of our final `devils_dr1.D10MasterRedshifts` catalogue in combination with the stellar masses taken from the `devils_dr1.D10ProSpectAGN` catalogue (see Section 7.1.3). Figure 14 show the redshift-stellar mass distribution of our final sample. We then also show the stellar mass completeness limits by calculating the point at which the spectroscopic sample drops below 85% completeness in comparison to the full photometric redshift sample. These lines are shown for a GAMA-like (r < 19.8) selection limit (orange), the COSMOS sample prior to DEVILS spectroscopic observations (red) and the final `devils_dr1.D10MasterRedshifts` sample (green). These lines can then be used to define a science-ready stellar-mass complete sample at a given epoch. In comparison to previous samples, the `devils_dr1.D10MasterRedshifts` sample allows stellar mass complete samples to be extended by ∼ 0.5 *dex* in stellar mass at all epochs out to z ∼ 1.

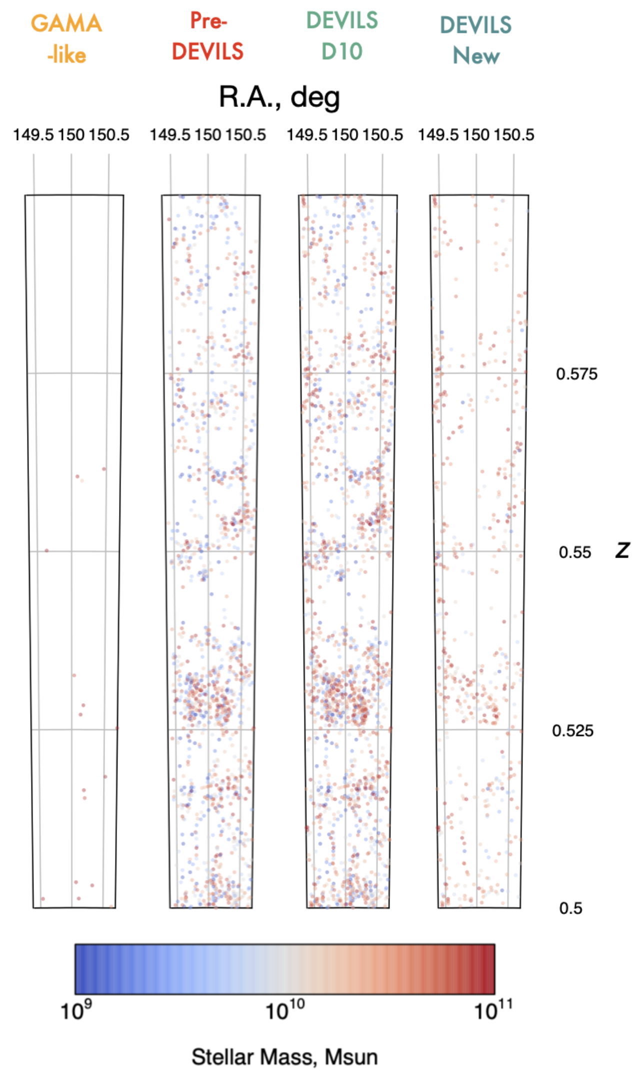

Figure 13. Light-cones showing large-scale-structure in the D10 region at $0.5<z<0.6$. Points are coloured by $\log_{10}$(stellar mass). Left shows the sample which would be obtained using GAMA-like spectroscopic limits (*.i.e.* comparable completeness sample at a brighter magnitude limit), where no large-scale-structure could be defined at these epochs. Middle-left shows the pre-DEVILS sample, where large-scale-structure is visible for the most massive structures, but a significant fraction of the population is missing. Middle-right shows the DEVILS D10 sample, where we are robustly tracing the large-scale-structure, including filaments, and identifying many more galaxies associated with each over-density (which will allow more robust dark matter halo measurements). Right shows the galaxies added by the DEVILS observations.

7 DR1 DATA PRODUCTS

In the following section we detail all of the DEVILS DR1 data products which are made publicly available via `Data Central`. These have been discussed in other key works, as such we do not go into detail regarding the derivation of these data products, we only present the data provided and notes how best to use said data.

7.1 Catalogues

Within the DEVILS DR1 we release 8 catalogues of measured and derived galaxy properties, discussed below. A unique identifier (`UID`) in applied to each photometric source. This `UID` is generated as `UID`=field number+round(`RAmax`*1000000) + | round(`DECmax`*1000000) |. For example, a source in the D10 region, at `RAmax`=149.717842907065 and `DECmax`=1.94849275929888 has a resultant UID=101497178431948496. Many of the DEVILS catalogue tables also contains a standard set of starting columns to allow easy selection of science-quality extra-galactic targets. These columns are outlined in Table 2. All tables described below can be accessed through the `Data Central` archive using a number of tools (Structured Query Language, Application Programming Interface, schema browser, etc) along with all meta data and documentation associated with the catalogue parameters.

7.1.1 *Photometric Measurements:* `devils_dr1.D10ProFoundPhotometry`

Photometric measurements and associated flags etc for the D10 sample are described extensively in Davies et al. (2021). Briefly, this work takes photometric data across 28 bands from the UV to FIR and measures source photometry using ProFound. Initial base segments are

Table 2. Base DR1 catalogue parameters used across multiple DR1 catalogues.

Name	Description	UCD	Unit	Type
UID	Unique identifier based on DEVILS filed, RA & DEC	meta.id	None	integer
RAcen	Right ascension position of the ProFound segment centre in the VISTA Y-band image	pos.eq.ra	deg	double
DECcen	Declination position of the segment centre in the VISTA Y-band image	pos.eq.ra	deg	double
RAmax	Right ascension position of the segment brightest pixel in the VISTA Y-band image	pos.eq.ra	deg	double
DECmax	Declination position of the segment brightest pixel in the VISTA Y-band image	pos.eq.ra	deg	double
mask	Flag to identify if the segment falls in a masked region. 0=not masked, >0=masked	meta.id	none	integer
artefactFlag	Flag to identify if the segment is an artefact (see Davies et al. (2021)). 0=Not artefact, >0=artefact	meta.id	none	integer
starFlag	Star/galaxy photometric classification (see Davies et al. (2021)). 0=galaxy, 1=star	meta.id	None	integer
mag_Y	Total magnitude measured in VISTA Y band segment	phot.mag;em.IR.Y	AB mag	double

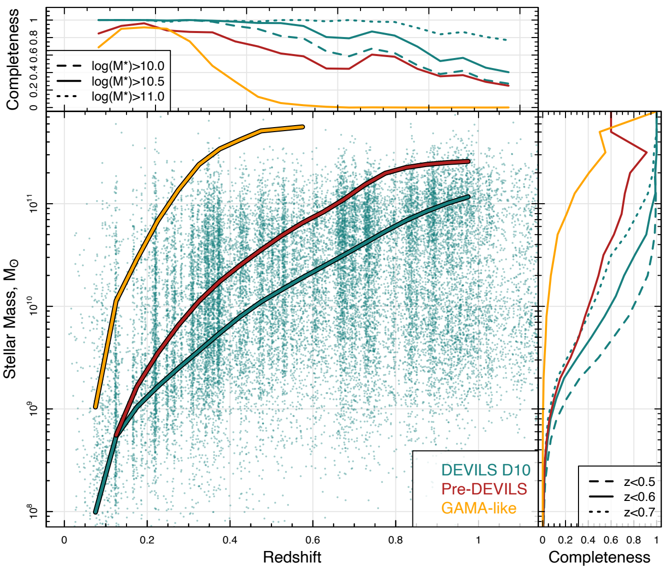

Figure 14. The resultant stellar mass - redshift distribution from combining the `devils_dr1.D10MasterRedshifts` catalogue and `devils_dr1.D10ProSpectAGN` catalogue. Top and side panels show the spectroscopic completeness as a function of redshift and stellar mass respectively. For DEVILS, these are shown for a range of stellar mass and redshift limits (given the respective legends). We show the samples obtained from a GAMA-like ($r < 19.8$) selection limit (orange), the COSMOS sample prior to DEVILS spectroscopic observations (red) and the final DEVILS D10 sample (green). To estimate the stellar mass - redshift completeness limits, we use the full photometric sample of objects and compare to those with spectroscopic redshifts. Lines in the main panel, are shown where the sample drops below 85% completeness. These lines can be used to define a stellar-mass complete sample at a given epoch. As such, in comparison to previous samples, the DEVILS D10 sample allows stellar mass complete samples to be extended by $\sim 0.5\,dex$ in stellar mass at all epochs out to $z \sim 1$.

defined using a deep Y+J+H+Ks stack from the UltraVISTA images. These segments are then used to measure photometry in UV through MIR imaging. In the FIR, PSF-based photometry is measured at the positions of 24μm-detected sources. Catalogues are then combined to provide multi-wavelength photometry for all sources detected in the NIR stack. This forms the base catalogue rows on which all other catalogues are generated. Following this, an object mask is defined excluding the regions around bright stars etc, and potential artefacts are flagged. Finally, sources are classified as either stars or galaxies based on their NIR colours, sizes and magnitudes. In the current data release we provide the full catalogues of these photometric measurements and flags as `devils_dr1.D10ProFoundPhotometry`. Columns in this catalogue (which are not already described in Table 2), are outlined in Table A1.

7.1.2 *Redshifts:* `devils_dr1.D10MasterRedshifts`

Redshift measurements detailed extensively in this paper are provided in catalogue `devils_dr1.D10MasterRedshifts`. This contains all redshift measurements discussed in Section 6. For each survey we include, from the original catalogue: the team-internal ID, R.A., Dec, redshift, flag or metric associated with redshift quality, and the redshift type (*i.e.* spec, grism, photo). In addition to the survey-specific redshift measurements, we then also include `zBest`, the survey source of the `zBest` (`zBestSource`) and the type of `zBest` (`zBestType`), based on the process outlined in Section 6. Columns in this catalogue (which are not already described in Table 2), are outlined in Table A3.

7.1.3 *SED Fitting:* `devils_dr1.D10ProSpectNoAGN` *&* `devils_dr1.D10ProSpectAGN`

SED fitting in the DEVILS D10 region is described extensively in Thorne et al. (2021) and Thorne et al. (2022). Briefly, Thorne et al. (2021) use the ProSpect (Robotham et al. 2020) SED fitting code to estimate galaxy properties such as stellar mass, SFR and star-formation history (SFH). In Thorne et al. (2022), this processes is updated to include an Active Galactic Nuclei (AGN) model, which allows for the identification of sources hosting bright AGN and improvements to the other derived properties for AGN host galaxies. The ProSpect analysis of Thorne et al. (2021, 2022) uses a parametric skewed-log-Normal truncated SFH for all galaxies, which assumes that all SFHs are smoothly evolving with look-back time. Note that between the publication of the Thorne et al works and the compilation of the redshift catalogues, 0.3% of sources changed their redshift assignment. The majority of these come from the DESI EDR, which was not publicly available at the time of the Thorne et al work. For this data release, we have re-run these objects though ProSpect using an identical set up to the Thorne et al work and updated the catalogue parameters. In our DR1 data release we provide both catalogues containing SED fit parameters for fits with and without a possible AGN model (`devils_dr1.D10ProSpectNoAGN` and `devils_dr1.D10ProSpectAGN` respectively). Columns in this catalogue (which are not already described in Table 2), are outlined in Tables A4 and A5.

7.1.4 *Visual Morphology:* `devils_dr1.D10VisualMorphology`

Visual morphological classifications are outlined in Hashemizadeh et al. (2021) who use HST-ACS imaging from the COSMOS survey (Scoville et al. 2007) to visually classify ~36,000 galaxies in

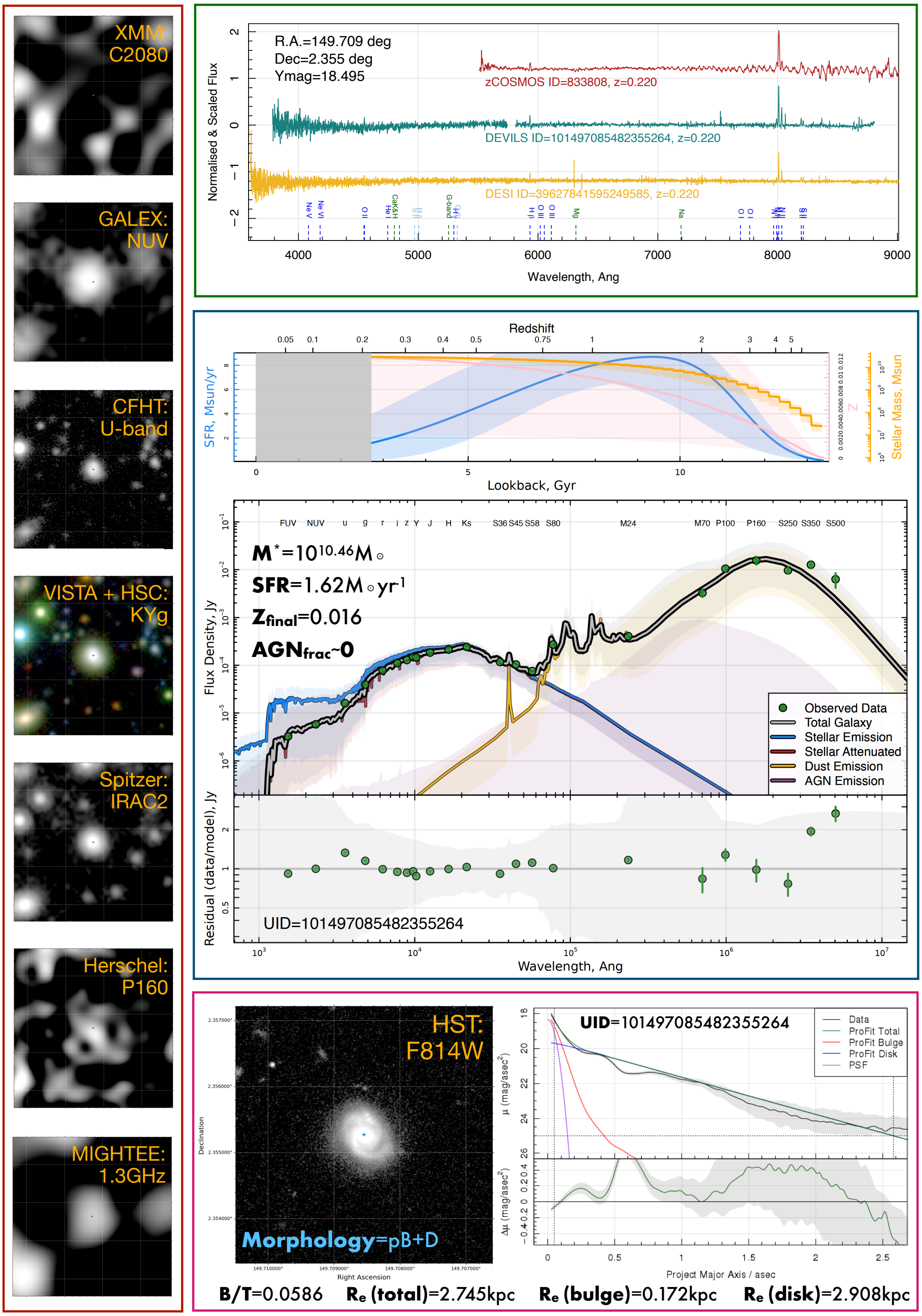

Figure 15. DEVILS DR1 data available for UID=101497085482355264. Left column displays selected imaging produced using the `Data Central` cutout tool. Top: spectroscopic observations from zCOSMOS, DEVILS-AAT and DESI-EDR. Middle: Output from the SED fitting presented in Thorne et al. (2022). In the bottom panel photometric data (including those from the left column) are shown in green. Photometry is fit with ProSpect for a stellar (blue line), dust (gold line) and AGN (purple line - in this case essentially zero) model. The stellar model is dust-attenuated to give the red line. Overall combined SED fit to the data is shown as the grey line, with residual shown in the bottom panel. Polygons show the upper and lower bounds of the MCMC chains produced in the fit. Resultant best-fit parameters for stellar mass, SFR, metallicity and AGN fraction are given. The top panel shows the best fit SFH (blue), stellar mass growth (orange) and metallicity evolution (pink). The x-axis here shows look-back time from today, such that the right-most edge of the grey-shaded region is the galaxy's observation epoch. Bottom: HST morphological and structural parameters. The left panel shows the HST image for this galaxy. In the morphological analysis of Hashemizadeh et al. (2021), this galaxy is visually classified as a pseudo bulge + disk (pB+D). In the right panel we show the ProFit structural decomposition of this galaxy from Cook et al. (2025), showing the radial surface brightness profile of bulge and disk components as a function of angular major axis, below the plot we show key structural parameters of the light-wighted bulge-to-total ratio (B/T), physical total/disk/bulge effective radius (R_e) in kpc.

the D10 region. Galaxies are selected for visual classification at $\log_{10}(M_\star/M_\odot)>9.5$ and $z<1.0$. Outside of this range of stellar mass even HST resolution imaging does not have adequate spatial resolution to visually constrain galaxy morphology, and above this redshift the traditional picture of galaxy morphological classes begins to break down as more and more galaxies become clumpy and asymmetric (both caused by true structural evolution and observational effects from observations probing bluer rest-frame emission). Galaxies within the sample limits are then classified as either elliptical, pure disk, disk + diffuse/pseudo bulge (pDB), disk + classical bulge (cBD), compact (too visually small to classify) and hard (asymmetric, merging, clumpy, extremely compact, and low-S/N systems) based on their F814W HST imaging. Galaxies were independently assessed by 4 classifiers, and objects with three or more votes in one category were adopted. Where classifiers disagreed, classes were debated until a consensus was obtained. Details of potential biases and systematics in this classification are described in Hashemizadeh et al. (2021). Columns in this catalogue (which are not already described in Table 2), are outlined in Table A7.

7.1.5 Structural Fitting: devils_dr1.D10ProFitStructure

Galaxy structural parameters in the D10 region are outlined in Cook et al. (2025). Briefly, this work used the ProFit (Robotham et al. 2017) and ProFuse (Robotham, Bellstedt, & Driver 2022) packages to decompose the F814W HST imaging for DEVILS galaxies into bulge and disk components and provide various Sérsic fitting parameters for each source such as Sérsic indices, sizes, bulge-to-total ratios and classifications based on the likelihood of the system being single- or two-component. Note that this analysis is once again only performed on $M_\star > 10^{9.5} M_\odot$ and $z<1.0$ galaxies. Columns in this catalogue (which are not already described in Table 2), are outlined in Table A6.

7.1.6 Group Environments: devils_dr1.D10GroupGals & devils_dr1.D10Groups

Finally, we also included catalogues detailing the group environmental metrics outlined in Bravo et al. (2025). Briefly, this work uses a similar approach to that outlined in Robotham et al. (2011) based on a bespoke friends-of-friends grouping algorithm. Bravo et al. (2025) optimises friends-of-friends linking lengths for DEVILS specifically and tests the success and failures of group recovery using updated DEVILS mock galaxy light cones from the SHARK semi-analytic model (Lagos et al. 2024). First, galaxies are linked to common halos and assigned a group ID and then group halo masses are measured from the galaxy kinematics, corrected to remove biases when compared to the mock galaxy light cones. Columns in this catalogue (which are not already described in Table 2), are outlined in Table A8 for the properties of group galaxies (*i.e.* group assignments, central/satellite classifications, group-centric locations) and Table A9 for the associated group properties (*i.e.* sizes, velocity dispersions, halo masses, etc).

7.2 Imaging

In addition to the catalogue photometric measurements for D10 galaxies, we also release all UV-FIR imaging from which this photometry is derived. Details of the majority of these imaging datasets are described extensively in Table 1 of Davies et al. (2021), and as such we do not recover them again here. However, we note that all imaging is standardised to the same D10 field size and pixel matched to the 0.15 arcsec/pixel VISTA-VIRCam UltraVISTA data. In addition to the imaging described in Davies et al. (2021) in our DR1 data release we also include XMM-Newton x-ray imaging for both C0520 and C2080 bands taken from the XXM-COSMOS survey program presented in Cappelluti et al. (2009), the HST imaging taken from the COSMOS survey (Scoville et al. 2007) mosaic images (this is not pixel-matched to UltraVISTA to retain the HST resolution imaging) and the 1.3 GHz radio continuum maps taken as part of the MeerKAT International Gigahertz Tiered Extragalactic Explorations (MIGHTEE, Jarvis et al. 2016) and detailed in Heywood et al. (2022). Full characteristics and details of this imaging are provided with the DEVILS DR1 release documentation on `Data Central`. This imaging can be accessed via various tools on the `Data Central` archive such as a multi-band and RGB cutout service, cone search and single object viewer.

7.3 Spectra

Finally we also provide flux and wavelength calibrated 1D spectra associated with DEVILS sources in the D10 region. These consist of the AAT+AAOmega spectra discussed in this paper, and publicly-available zCOSMOS (Lilly et al. 2007) and DESI EDR (DESI Collaboration et al. 2024) spectra where available. Spectra are tagged to a specific DEVILS UID, standardised to the same wavelength scale and converted to the same format with the same header keywords. Details of this format and associated meta data are made available via `Data Central`. The spectra can also be dynamically visualised through the `Data Central` single object viewer and/or downloaded directly from the `Data Central` archive.

To highlight the breadth of data available for this sample, in Figure 15 we show a summary overview of the data products available in the DEVILS DR1 data release for a single source (UID=101497085482355264). This comprises of examples of multi-wavelength imaging (left), 1D spectra from DEVILS-AAT, zCOSMOS and DESI-EDR (top), SED fits and associated parameters (middle), and morphological and structural characteristics (bottom). In Figure 16, we then show an example of group diagnostics for a group in the D10 region (GroupID=100012). Data of this quality and scope exists for a large fraction of sources in the DEVILS DR1 data release.

8 THE STAR-FORMATION - DENSITY RELATION AT INTERMEDIATE REDSHIFT

In the final parts of this paper, we highlight the power of the extensive data set available in the DEVILS DR1 data release by exploring the impact of local galaxy density on the star-formation in galaxies, split by both stellar mass and morphology. We choose this science case as it utilises the DR1 photometric catalogues (`devils_dr1.D10ProFoundPhotometry`), redshift catalogue (`devils_dr1.D10MasterRedshifts`), SED fitting catalogue (`devils_dr1.D10ProSpectAGN`) and morphology catalogue (`devils_dr1.D10VisualMorphology`). These results are simply designed to highlight the power of combining data from the DEVILS DR1 data release to produce new and interesting results, to supplement the existing body of work already published using the DEVILS DR1 data.

Briefly, galaxies can be broadly classified into two main categories: blue, gas-rich, star-forming systems, and red, gas-poor, quiescent systems with little or no ongoing star formation (e.g., Blanton

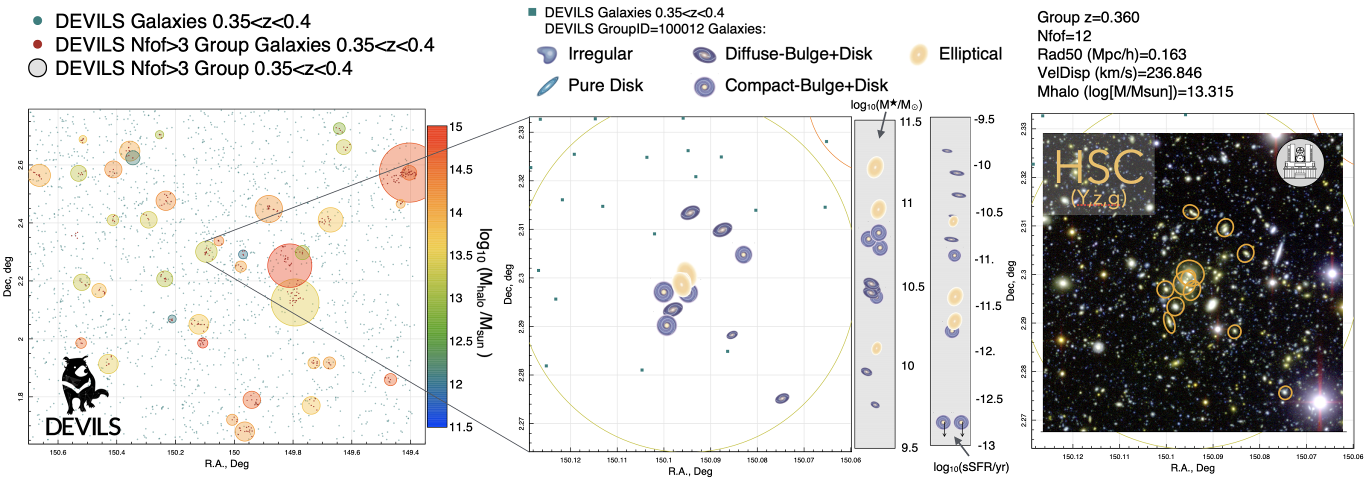

Figure 16. Example of group diagnostics available in DEVILS DR1. Left shows the distribution of isolated galaxies (green points), group galaxies (red points) and dark matter haloes (coloured circles) at 0.35<z<0.4. Halos are coloured by halo mass, and their circle size represents the group physical extent. Middle shows a zoom in on group 100012. Group galaxies are now shown based on their morphological type, and grey bars show the stellar mass and SFR distribution of the group galaxies. Right shows the Subaru HSC Yzg image of the group, with group galaxies shown in orange. Key group measurements are given above the image.

et al. 2003; Kauffmann et al. 2003a, 2004; Baldry et al. 2004; Balogh et al. 2004; Brinchmann et al. 2004; Taylor et al. 2015; Davies et al. 2019b). Throughout the history of the Universe, the relative abundance of galaxies in these two categories has evolved significantly. All galaxies are believed to begin as low-mass, blue, star-forming systems, gradually transitioning into quiescent systems over time (e.g., Bell et al. 2004; Faber et al. 2007; Martin et al. 2007). This transformation is ongoing, with an increasing fraction of galaxies becoming quiescent as the Universe ages. Eventually, star formation is expected to cease entirely, leaving all galaxies in a passive state. One of the primary drivers of galaxy quenching is local environment. In dense environments—such as galaxy clusters, groups, or even close galaxy pairs (see Patton et al. 2011; Robotham et al. 2014; Davies et al. 2016)—the supply of cold gas needed for ongoing star formation can be heated, disrupted or removed, ultimately leading to quenching (e.g., Peng et al. 2010, 2012; McGee, Bower, & Balogh 2014; Haines et al. 2015; Schaefer et al. 2017; Bluck et al. 2020a,b; Cortese, Catinella, & Smith 2021; Cleland & McGee 2021). A variety of physical mechanisms can contribute to this process, including ram-pressure stripping and tidal interactions (Gunn & Gott 1972; Moore et al. 1999; Poggianti et al. 2017; Brown et al. 2017; Barsanti et al. 2018), strangulation (or starvation) (Larson, Tinsley, & Caldwell 1980; Moore et al. 1999; Peng et al. 2015; Nichols & Bland-Hawthorn 2011), and galaxy harassment (Moore et al. 1996).

Many studies have found a strong correlation between suppression of star-formation and over-dense environments, witnessing environmental quenching in action (*e.g.* Wetzel et al. 2013; Barsanti et al. 2018; Oxland et al. 2024; Davies et al. 2019b, 2025c). However, most of these studies are limited to the local Universe, and as such open questions remain as to the ubiquity of environmental quenching at earlier times. Some works have studied the impact of environment on galaxies at earlier times. However, these works focus on using sparse spectroscopic redshifts and/or photometric redshift-dominated samples (*e.g.* Fossati et al. 2017; Peng et al. 2010) or target the most over-dense and extreme environments (*e.g.* Butcher & Oemler 1984; Muzzin et al. 2014; Haines et al. 2015; Foltz et al. 2018; van der Burg et al. 2020; Turner et al. 2021; Mao et al. 2022; Siudek et al. 2022; Figueira et al. 2024). In addition, it is also well-known that stellar mass, star formation and galaxy morphological types all correlate with environment (Bamford et al. 2009; Alpaslan et al. 2015; van der Wel et al. 2010; Pfeffer et al. 2023; Davies et al. 2025a,b,d). As such, to disentangle the impact of environment on the star-forming properties of galaxies alone, we must also control for the varying distribution of both stellar mass and morphology as a function of environment.

Here we utilise the DEVILS DR1 sample described in this paper to explore the impact of over-dense environments on star-formation at intermediate redshift (0.2<z<0.5) and in more typical environments. We then split this sample as a function of stellar mass and morphology, to determine if star-formation suppression in over-dense environments is a ubiquitous feature of the galaxy population, or limited to a specific stellar mass or morphological type.

First, we take all DEVILS DR1 galaxies at intermediate redshift (0.2<z<0.5) and 10<$\log_{10}(M_\star/M_\odot)$<11 (*i.e.* above the 80% spectroscopic completeness limits at all epochs in Figure 14) and for a relatively narrow range of stellar masses. This allows us to study the suppression of star-formation in a controlled and largely stellar-mass complete sample. Next, to define the local galaxy density for this sample, we take each galaxy in turn and only consider sources within a radial velocity separation of $\pm 1000\,\mathrm{km\,s^{-1}}$ (*e.g.* as in Baldry et al. 2006). We then calculate the projected local galaxy density as:

$$\Sigma_N = \frac{N}{\pi d_N^2}, \mathrm{Mpc}^{-2} \qquad (2)$$

where d_N is the projected distance to the Nth nearest neighbour. In our analysis we calculate this for the 1st (*i.e* separation to closest neighbour), 3rd, 5th and 7th nearest neighbour (Σ_1, Σ_3, Σ_5, Σ_7). We initially explore this using a range of Σ_N values, to show that the choice of N does not significantly impact our results.

We then bin the sample in $\Delta\log_{10}(\Sigma_N)$=0.5 bins, and measure the median SFR and stellar mass of galaxies in each bin. In Figure 17 as black points/lines we show the median SFR as a function of Σ_N in

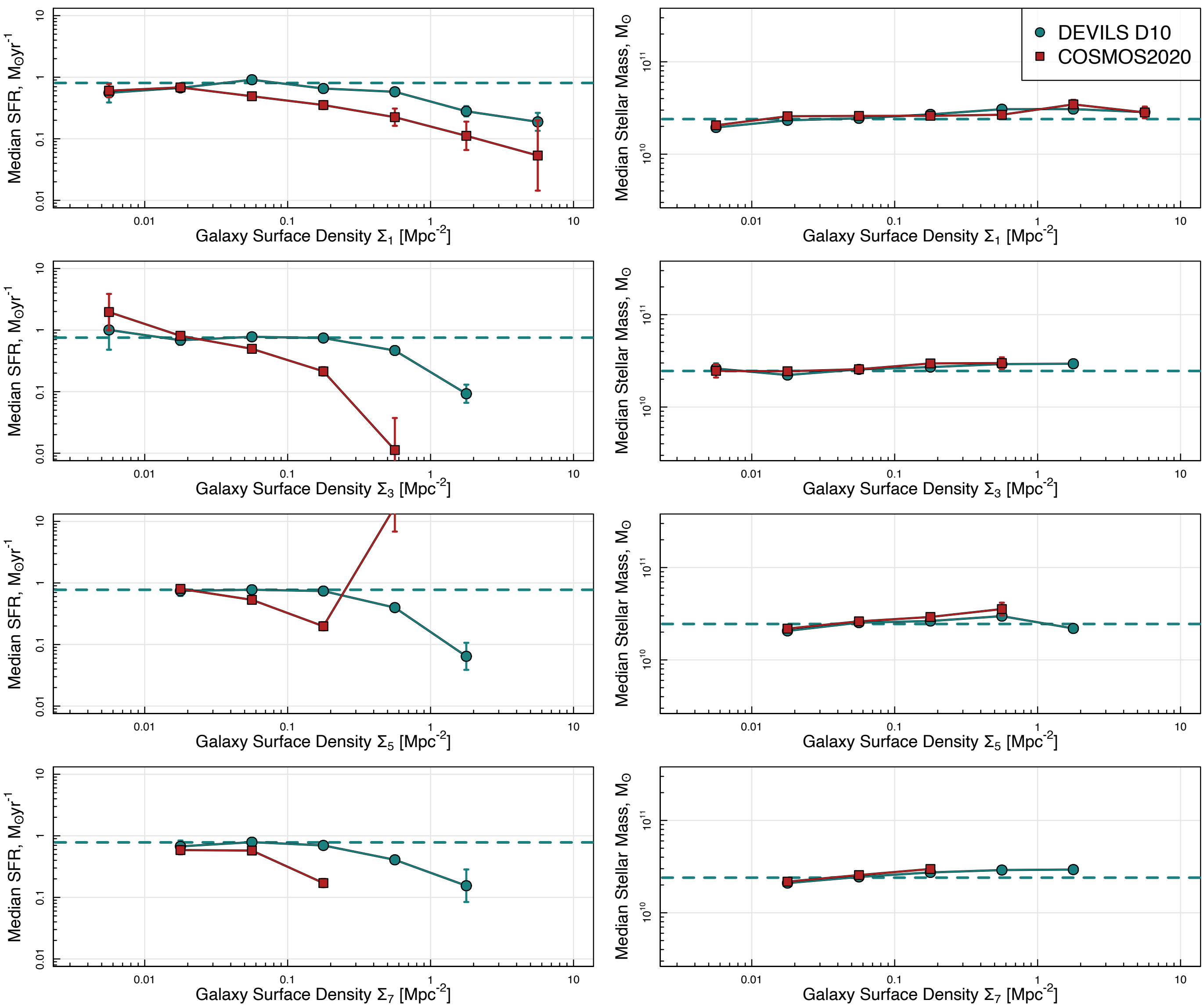

Figure 17. The median SFR (left column) and stellar mass (right column) of $10<\log_{10}(M_\star/M_\odot)<11$ as a function of nearest-neighbour density, Σ_N, for DEVILS galaxies at $0.2<z<0.5$ (black) and COSMOS2020 galaxies with the same selection (red - see text for details). The dashed horizontal lines show the median value for all galaxies with $\Sigma_N < 0.1$ (*i.e.* isolated systems) in DEVILS. Error bars are calculated as the standard error on the median ($\sigma/\sqrt{\#}$, where # is the number of galaxies in the bin). Rows show nearest-neighbour density calculated for different N^{th} nearest neighbours. Only bins containing ≥10 galaxies are shown. In DEVILS strong trends are observed of SFR decreasing with local density and weak trends of stellar mass increasing with local density. While these trends are also found in the COSMOS2020 catalogue, particularly at low Σ_N, photometric redshift samples have larger errors and show different level of suppression to the full spectroscopic DEVILS sample.

the left column and median stellar mass as a function of Σ_N in the right column. Rows show the different values of N used to calculate Σ_N. Error bars are calculated as the standard error on the median and only bins containing >10 galaxies are plotted. The black dashed horizontal line shows the median values for all isolated galaxies (defined as $\Sigma_N<0.1$). We see that for all metrics of Σ_N, there is a decline in median SFR with increasing galaxy density. Median SFRs are relatively constant at $\sim 0.8\mathrm{M}_\odot\,\mathrm{yr}^{-1}$ until the local galaxy density reaches above $\sim 0.2\,\mathrm{Mpc}^{-2}$, where we then see a decline of ~1 dex in median SFRs to the most over-dense regions. In the right column, we see that there is a weak trend of the median stellar mass increasing slight as we move to higher density environment. However, for the fixed stellar mass sample used here ($10<\log_{10}(M_\star/M_\odot)<11$), this change is small, and not as significant as the change seen in the median SFR. First this indicates that high-density environments are having an impact on star-formation in the overall galaxy population at $0.2<z<0.5$, and that this suppression can be observed irrespective of the choice of Σ_N. This is consistent with the interpretation that over-dense environments lead to the suppression of star-formation via processes such as stripping, tidal interactions, starvation, etc.

To highlight the power of our highly-complete spectroscopic sample in DEVILS when exploring the environmental impact on galaxy evolution, we repeat the process above using the publicly available COSMOS2020 catalogue in the COSMOS region Weaver et

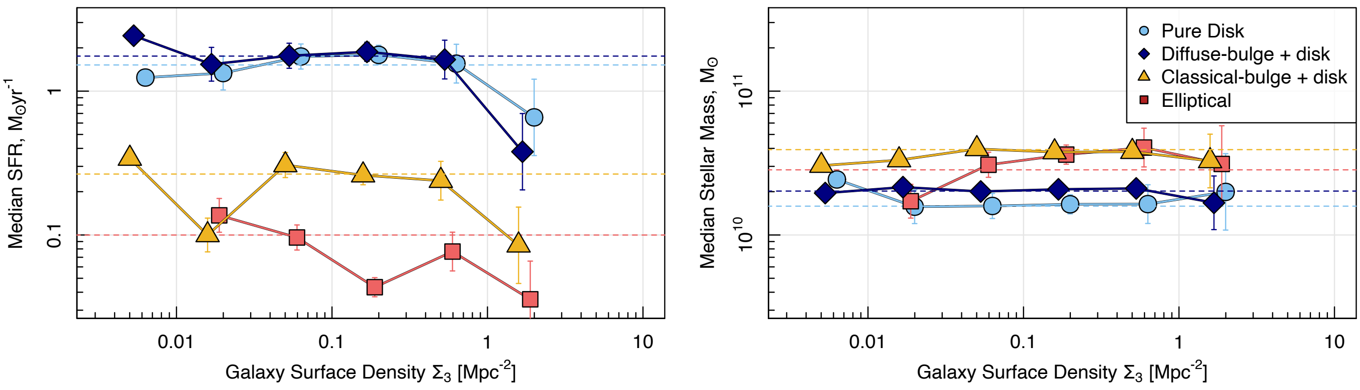

Figure 18. The same as Figure 17, but now split into individual morphological classes. We see suppression of star-formation in high density environments for all morphological classes.

al. (2022). First we take all sources that are flagged as having good photometry as `FLAG_COMBINED=0`. The COSMOS2020 catalogue provides LePhare best-fit photometric redshifts, stellar masses and SFRs (Ilbert et al. 2006). We then repeat the process outlined in the previous paragraph selecting the same stellar mass and redshift range, and determining local galaxy densities in an identical manner. We note that we cannot easily supplement this with the spectroscopic redshift catalogue in COSMOS as stellar masses and SFRs are calculated assuming the photometric redshift is correct. In Figure 17 we then also show median SFR and stellar mass as a function of local density for the COSMOS2020 sample as red points/lines. While we do see evidence of SFR suppression in over-dense environments for Σ_1 and Σ_3 local density metrics, these have larger errors than seen in the DEVILS D10 sample, and are only very weakly observed at higher values of Σ_N. We also find that the observed strength of the impact of local over-density on star-formation in galaxies differs significantly between these samples, where the photometric redshift samples of the COSMOS2020 catalogue over-estimate the decline in median SFR at higher over-densities in comparison to DEVILS. This could be due to differences in the SED fitting approaches. However, the fact that the weak trends between stellar mass and local environmental density are very similar between the two samples, and the median SFRs at low density environments are very similar, potentially suggests that some of this difference is driven by the use of photometric redshifts over spectroscopic sample to define local density. We also note that using the metric for local galaxy density defined above may bias any results derived from photometric redshifts alone. Errors on photometric redshifts are typically >1000 km s^{-1}, and thus excluding galaxies above ±1000 km s^{-1} in our local galaxy density calculation, may miss true galaxy nearest neighbours with large photometric redshift errors. This will typically lead to local galaxy densities being underestimated. However, if we relax this constraint to ±5000 km s^{-1} for the COSMOS2020 sample, the results do not significantly change. In combination, this indicates that less-biased and highly complete spectroscopic samples are essential in determining the environmental impact on galaxy evolution.

Following this, we can now also utilise the `devils_dr1.D10VisualMorphology` catalogue to split this sample based on morphological type (which cannot be undertaken for the COSMOS2020 sample). In Figure 18 we display the median SFR and stellar mass as a function of Σ_3, now split by individual visual morphological types. We note that other Σ_N values show similar trends. Here we see that the decline in median SFR in higher density environments remains for all morphological types. This suggests that the suppression in star-formation in over-dense environments is not limited to a specific galaxy type, or is driven by the varying contributions of different morphological types as a function of environment (*e.g.* Davies et al. 2025d).

However, we do see that potentially different morphological classes have different trends with galaxy surface density. Elliptical and disk + classical bulge morphological types shows a gradual decline in median SFR with increasing over-density while pure disk and disk + diffuse/pseudo bulge galaxies only show a decline in median SFR in the most over-dense bin. We do also see a weak trend of stellar masses increasing towards over-dense environments for the elliptical population, which could potentially drive some of this result (as higher stellar mass galaxies have lower SFRs). However, it does appear that the suppression of star-formation in high density environments is not limited to a specific morphological type and is seen in all classes.

Finally, to explore how changes in the stellar mass distribution as a function of local over-density may impact these trends, in Figure 19, we then split our sample further into two stellar mass ranges, and show panels split by morphological type. Here we see that in both stellar mass ranges the full sample of all morphologies (top row) displays a suppression of star-formation. We now also see no trend in stellar mass as a function of local galaxy density - indicating this is a true environmental effect on star-formation. We also find that this suppression of star-formation in over-dense environments is also observed when split by both morphological type and stellar mass, *i.e.* there is a decline in median star formation in higher density environments at all stellar mass and morphologies. However, for all morphological classes, we do find that lower stellar mass galaxies appear more impacted by their environment - showing a greater degree of suppression.

Overall, these result indicate that the suppression of star-formation (quenching) in over-dense environments is a ubiquitous feature of the Universe at $0.2<z<0.5$) and $10<\log_{10}(M_\star/M_\odot)<11$, occurring at a range of stellar masses and in all morphological types. We also find that lower stellar mass galaxies show more suppression than higher stellar mass galaxies for all morphological types. This is likely expected as the processes which lead to quenching in satellite galaxies (ram-pressure stripping, tidal interactions, etc) are likely dependant on satellite stellar mass, where in a fixed mass halo, lower stellar mass galaxies are more likely to impacted by these processes.

9 CONCLUSIONS

In this work we present the first data release of the Deep Extragalactic VIsible Legacy Survey, covering all data products in the D10 (COSMOS) region. We discuss the spectroscopic DEVILS observations at the AAT and completion of the main redshift catalogues used in DEVILS science papers - providing 4,859 new unique spectroscopic redshifts for faint sources in the COSMOS region. We then outline details of all data products which are made available including catalogues of measure/derived properties, imaging and 1D spectra. All data is made available through `Data Central` (datacentral.org.au). Finally we highlight a scientific application of this extensive data set, exploring the suppression of star-formation in over-dense environments at intermediate redshift (0.2<z<0.5) when split by both stellar mass and visual morphology.

ACKNOWLEDGEMENTS

LJMD acknowledges support from the Australian Research Councils Future Fellowship and Discovery Project schemes (FT200100055 and DP250104611). ASGR, and SB acknowledge support from the Australian Research Council's Future Fellowship scheme (FT200100375). MB is funded by McMaster University through the William and Caroline Herschel Fellowship. M.S. acknowledges support by the State Research Agency of the Spanish Ministry of Science and Innovation under the grants 'Galaxy Evolution with Artificial Intelligence' (PGC2018-100852-A-I00) and 'BASALT' (PID2021-126838NB-I00) and the Polish National Agency for Academic Exchange (Bekker grant BPN/BEK/2021/1/00298/DEC/1). This work was partially supported by the European Union's Horizon 2020 Research and Innovation program under the Maria Sklodowska-Curie grant agreement (No. 754510). Parts of this research were conducted by the Australian Research Council Centre of Excellence for All Sky Astrophysics in 3 Dimensions (ASTRO 3D), through project number CE170100013. DEVILS is an Australian project based around a spectroscopic campaign using the Anglo-Australian Telescope. DEVILS is part funded via Discovery Programs by the Australian Research Council and the participating institutions. The DEVILS website is devils.research.org.au. This paper includes data that has been provided by the AAO `Data Central` Science Platform (datacentral.org.au).

10 DATA AVAILABILITY

All data products used in this paper are made available through the Data Central (datacentral.org.au) archive.

REFERENCES

Abazajian K. N., Adelman-McCarthy J. K., Agüeros M. A., Allam S. S., Allende Prieto C., An D., Anderson K. S. J., et al., 2009, ApJS, 182, 543. doi:10.1088/0067-0049/182/2/543
Adams N. J., Bowler R. A. A., Jarvis M. J., Häußler B., McLure R. J., Bunker A., Dunlop J. S., et al., 2020, MNRAS, 494, 1771. doi:10.1093/mnras/staa687
Alam S., Ata M., Bailey S., Beutler F., Bizyaev D., Blazek J. A., Bolton A. S., et al., 2017, MNRAS, 470, 2617. doi:10.1093/mnras/stx721
Alarcon A., Gaztanaga E., Eriksen M., Baugh C. M., Cabayol L., Casas R., Carretero J., et al., 2021, MNRAS, 501, 6103. doi:10.1093/mnras/staa3659
Alpaslan M., Driver S., Robotham A. S. G., Obreschkow D., Andrae E., Cluver M., Kelvin L. S., et al., 2015, MNRAS, 451, 3249. doi:10.1093/mnras/stv1176
Arnouts S., Ilbert O., 2011, ascl.soft. ascl:1108.009
Baldry, I. K., Glazebrook, K., Brinkmann, J., et al. 2004, ApJ, 600, 681
Baldry I. K., Balogh M. L., Bower R. G., Glazebrook K., Nichol R. C., Bamford S. P., Budavari T., 2006, MNRAS, 373, 469. doi:10.1111/j.1365-2966.2006.11081.x
Baldry I. K., Robotham A. S. G., Hill D. T., Driver S. P., Liske J., Norberg P., Bamford S. P., et al., 2010, MNRAS, 404, 86. doi:10.1111/j.1365-2966.2010.16282.x
Baldry I. K., Alpaslan M., Bauer A. E., Bland-Hawthorn J., Brough S., Cluver M. E., Croom S. M., et al., 2014, MNRAS, 441, 2440. doi:10.1093/mnras/stu727
Balogh, M., Eke, V., Miller, C., et al. 2004, MNRAS, 348, 1355
Bamford S. P., Nichol R. C., Baldry I. K., Land K., Lintott C. J., Schawinski K., Slosar A., et al., 2009, MNRAS, 393, 1324. doi:10.1111/j.1365-2966.2008.14252.x
Barsanti, S., Owers, M. S., Brough, S., et al. 2018, ApJ, 857, 71
Bell, E. F., Wolf, C., Meisenheimer, K., et al. 2004, ApJ, 608, 752
Belli S., Newman A. B., Ellis R. S., 2015, ApJ, 799, 206. doi:10.1088/0004-637X/799/2/206
Bellstedt S., Driver S. P., Robotham A. S. G., Davies L. J. M., Bogue K. R. J., Cook R. H. W., Hashemizadeh A., et al., 2020, MNRAS, 496, 3235. doi:10.1093/mnras/staa1466
Bellstedt S., Robotham A. S. G., Driver S. P., Thorne J. E., Davies L. J. M., Lagos C. del P., Stevens A. R. H., et al., 2020, MNRAS, 498, 5581. doi:10.1093/mnras/staa2620
Blake, C., Amon, A., Childress, M., et al. 2016, MNRAS, 462, 4240
Blanton, M. R., Hogg, D. W., Bahcall, N. A., et al. 2003, ApJ, 594, 186
Bluck A. F. L., Maiolino R., Sánchez S. F., Ellison S. L., Thorp M. D., Piotrowska J. M., Teimoorinia H., et al., 2020a, MNRAS, 492, 96. doi:10.1093/mnras/stz3264
Bluck A. F. L., Maiolino R., Piotrowska J. M., Trussler J., Ellison S. L., Sánchez S. F., Thorp M. D., et al., 2020b, MNRAS, 499, 230. doi:10.1093/mnras/staa2806
Brinchmann, J., Charlot, S., White, S. D. M., et al. 2004, MNRAS, 351, 1151
Brammer G. B., van Dokkum P. G., Coppi P., 2008, ApJ, 686, 1503. doi:10.1086/591786
Bravo M., Davies L. J. M., Robotham A. S. G., Lagos C. del P., Bellstedt S., Bland-Hawthorn J., Siudek M., et al., 2025, arXiv, arXiv:2509.13530. doi:10.48550/arXiv.2509.13530
Brown T., et al., 2017, MNRAS, 466, 1275
Butcher H., Oemler A., 1984, ApJ, 285, 426. doi:10.1086/162519
Cameron E., Driver S. P., 2007, MNRAS, 377, 523. doi:10.1111/j.1365-2966.2007.11507.x
Cappelluti N., Brusa M., Hasinger G., Comastri A., Zamorani G., Finoguenov A., Gilli R., et al., 2009, A&A, 497, 635. doi:10.1051/0004-6361/200810794
Carter D., Metcalfe N., 1980, MNRAS, 191, 325. doi:10.1093/mnras/191.2.325
Childress M. J., et al., 2017, MNRAS, 472, 273
Cirasuolo M., Fairley A., Rees P., Gonzalez O. A., Taylor W., Maiolino R., Afonso J., et al., 2020, Msngr, 180, 10. doi:10.18727/0722-6691/5195
Cleland C., McGee S. L., 2021, MNRAS, 500, 590. doi:10.1093/mnras/staa3267
Colless M., Dalton G., Maddox S., Sutherland W., Norberg P., Cole S., Bland-Hawthorn J., et al., 2001, MNRAS, 328, 1039. doi:10.1046/j.1365-8711.2001.04902.x
Comparat J., Richard J., Kneib J.-P., Ilbert O., Gonzalez-Perez V., Tresse L., Zoubian J., et al., 2015, A&A, 575, A40. doi:10.1051/0004-6361/201424767
Cortese L., Catinella B., Smith R., 2021, PASA, 38, e035. doi:10.1017/pasa.2021.18
Cook R. H. W., Davies L. J. M., Bellstedt S., Robotham A. S. G., Driver S. P.,

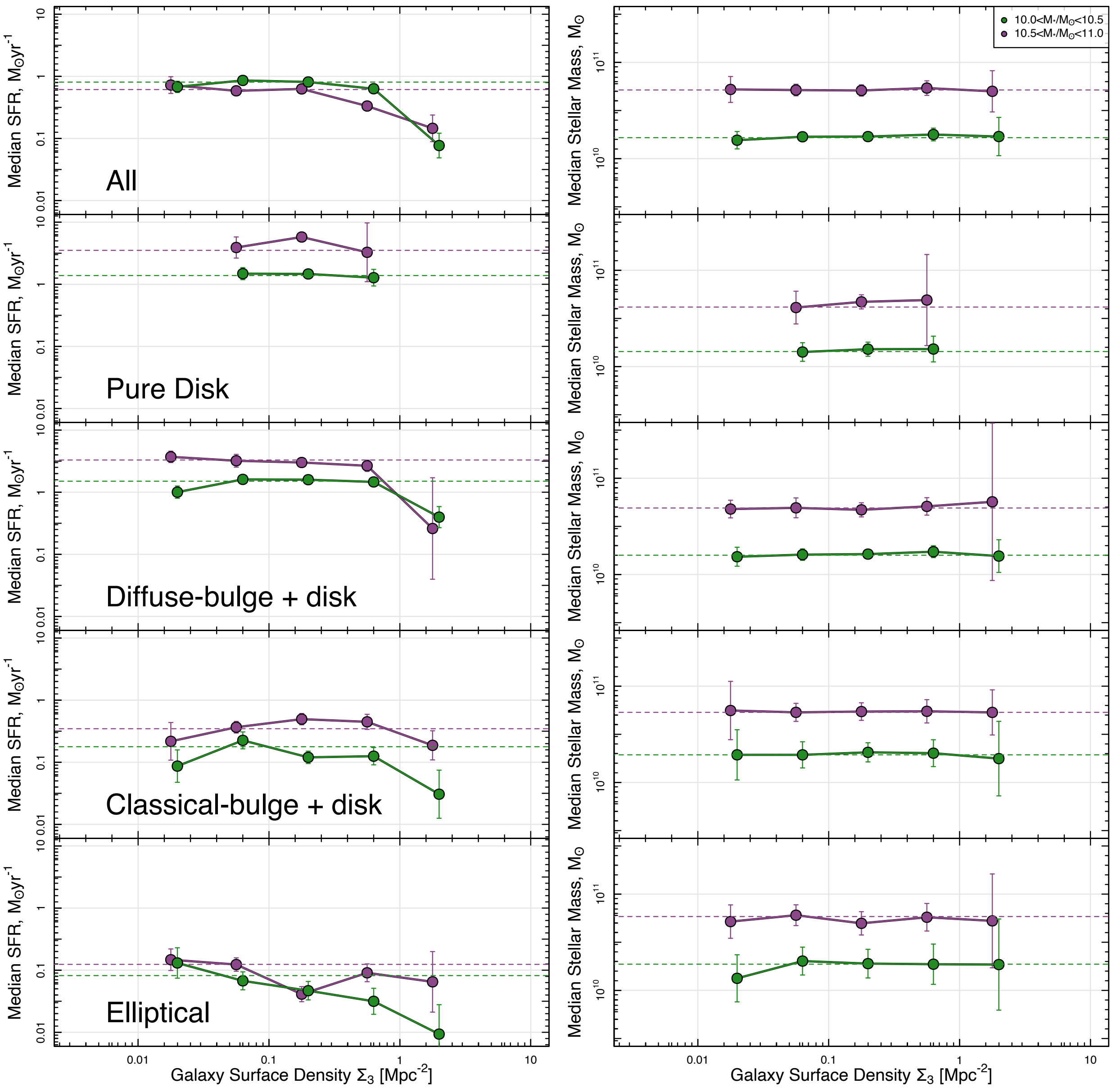

Figure 19. Similar to Figure 17, but now split into two different stellar mass ranges and showing all morphological types separately. Given the smaller number of galaxies in this sub-selection, we relax our criteria to show all bins containing ≥5 galaxies. We find typically higher level of suppression in lower stellar mass galaxies, even when controlled for morphological type.

Siudek M., Wolf C., 2025, MNRAS.tmp. doi:10.1093/mnras/staf575

Cool R. J., Moustakas J., Blanton M. R., Burles S. M., Coil A. L., Eisenstein D. J., Wong K. C., et al., 2013, ApJ, 767, 118. doi:10.1088/0004-637X/767/2/118

Cooper M. C., Griffith R. L., Newman J. A., Coil A. L., Davis M., Dutton A. A., Faber S. M., et al., 2012, MNRAS, 419, 3018. doi:10.1111/j.1365-2966.2011.19938.x

Croom S., Saunders W., Heald R., 2004, AAONw, 106, 12

Damjanov I., Zahid H. J., Geller M. J., Fabricant D. G., Hwang H. S., 2018, ApJS, 234, 21

Davies L. J. M., Driver S. P., Robotham A. S. G., Baldry I. K., Lange R., Liske J., Meyer M., et al., 2015, MNRAS, 447, 1014. doi:10.1093/mnras/stu2515

Davies L. J. M., Robotham A. S. G., Driver S. P., Alpaslan M., Baldry I. K., Bland-Hawthorn J., Brough S., et al., 2015, MNRAS, 452, 616. doi:10.1093/mnras/stv1241

Davies L. J. M., Robotham A. S. G., Driver S. P., Alpaslan M., Baldry I. K., Bland-Hawthorn J., Brough S., et al., 2016, MNRAS, 455, 4013. doi:10.1093/mnras/stv2573

Davies L. J. M., Driver S. P., Robotham A. S. G., Grootes M. W., Popescu C. C., Tuffs R. J., Hopkins A., et al., 2016, MNRAS, 461, 458. doi:10.1093/mnras/stw1342

Davies L. J. M., et al., 2018, MNRAS, 480, 768

Davies L. J. M., Robotham A. S. G., Lagos C. del P., Driver S. P., Stevens A. R. H., Bahé Y. M., Alpaslan M., et al., 2019, MNRAS, 483, 5444. doi:10.1093/mnras/sty3393

Davies L. J. M., Thorne J. E., Robotham A. S. G., Bellstedt S., Driver S. P., Adams N. J., Bilicki M., et al., 2021, MNRAS, 506, 256.

doi:10.1093/mnras/stab1601
Davies L. J. M., Thorne J. E., Bellstedt S., Bravo M., Robotham A. S. G., Driver S. P., Cook R. H. W., et al., 2022, MNRAS, 509, 4392. doi:10.1093/mnras/stab3145
Davies L. J. M., Thorne J. E., Bellstedt S., Cook R. H. W., Bravo M., Robotham A. S. G., Lagos C. del P., et al., 2025, MNRAS, 540, 1870. doi:10.1093/mnras/staf693
Davies L. J. M., Thorne J. E., Bellstedt S., Cook R. H. W., Bravo M., Robotham A. S. G., Lagos C. del P., et al., 2025, MNRAS, 541, 573. doi:10.1093/mnras/staf872
Davies L. J. M., et al., 2025c, MNRAS, xxx,xxx
Davies L. J. M., et al., 2025c, MNRAS, xxx,xxx
DESI Collaboration, Adame A. G., Aguilar J., Ahlen S., Alam S., Aldering G., Alexander D. M., et al., 2024, AJ, 168, 58. doi:10.3847/1538-3881/ad3217
van Dokkum P. G., Franx M., 1996, MNRAS, 281, 985. doi:10.1093/mnras/281.3.985
Drinkwater, M. J., Byrne, Z. J., Blake, C., et al. 2018, MNRAS, 474, 4151
Driver S. P., Hill D. T., Kelvin L. S., Robotham A. S. G., Liske J., Norberg P., Baldry I. K., et al., 2011, MNRAS, 413, 971. doi:10.1111/j.1365-2966.2010.18188.x
Driver S. P., Liske J., Davies L. J. M., Robotham A. S. G., Baldry I. K., Brown M. J. I., Cluver M., et al., 2019, Msngr, 175, 46. doi:10.18727/0722-6691/5126
Driver S. P., Bellstedt S., Robotham A. S. G., Baldry I. K., Davies L. J., Liske J., Obreschkow D., et al., 2022, MNRAS, 513, 439. doi:10.1093/mnras/stac472
Driver S. P., Robotham A. S. G., Obreschkow D., Peacock J. A., Baldry I. K., Bellstedt S., Bland-Hawthorn J., et al., 2022, MNRAS, 515, 2138. doi:10.1093/mnras/stac581
D'Silva J. C. J., Driver S. P., Lagos C. D. P., Robotham A. S. G., Bellstedt S., Davies L. J. M., Thorne J. E., et al., 2023, MNRAS, 524, 1448. doi:10.1093/mnras/stad1974
de Jong R. S., et al., 2014, SPIE, 9147, 91470M
Faber, S. M., Willmer, C. N. A., Wolf, C., et al. 2007, ApJ, 665, 265
Figueira M., Siudek M., Pollo A., Krywult J., Vergani D., Bolzonella M., Cucciati O., et al., 2024, A&A, 687, A117. doi:10.1051/0004-6361/202347774
Foltz R., Wilson G., Muzzin A., Cooper M. C., Nantais J., van der Burg R. F. J., Cerulo P., et al., 2018, ApJ, 866, 136. doi:10.3847/1538-4357/aad80d
Fossati M., Wilman D. J., Mendel J. T., Saglia R. P., Galametz A., Beifiori A., Bender R., et al., 2017, ApJ, 835, 153. doi:10.3847/1538-4357/835/2/153
Fuenblackba-Fuentes M. F., Davies L. J. M., Robotham A. S. G., Cook R. H. W., Bellstedt S., Lagos C. D. P., Bravo M., et al., 2025, MNRAS, 539, 1651. doi:10.1093/mnras/staf596
Gadotti D. A., 2009, MNRAS, 393, 1531. doi:10.1111/j.1365-2966.2008.14257.x
Gadotti D. A., Kauffmann G., 2009, MNRAS, 399, 621. doi:10.1111/j.1365-2966.2009.15328.x
Garilli B., Fumana M., Franzetti P., Paioro L., Scodeggio M., Le Fèvre O., Paltani S., et al., 2010, PASP, 122, 827. doi:10.1086/654903
Garilli B., Guzzo L., Scodeggio M., Bolzonella M., Abbas U., Adami C., Arnouts S., et al., 2014, A&A, 562, A23. doi:10.1051/0004-6361/201322790
Greene J., Bezanson R., Ouchi M., Silverman J., the PFS Galaxy Evolution Working Group, 2022, arXiv, arXiv:2206.14908. doi:10.48550/arXiv.2206.14908
Gunawardhana M. L. P., Hopkins A. M., Sharp R. G., Brough S., Taylor E., Bland-Hawthorn J., Maraston C., et al., 2011, MNRAS, 415, 1647. doi:10.1111/j.1365-2966.2011.18800.x
Gunn J. E., Gott J. R., III, 1972, ApJ, 176, 1
Hahn C., Wilson M. J., Ruiz-Macias O., Cole S., Weinberg D. H., Moustakas J., Kremin A., et al., 2023, AJ, 165, 253. doi:10.3847/1538-3881/accff8
Haines C. P., Pereira M. J., Smith G. P., Egami E., Babul A., Finoguenov A., Ziparo F., et al., 2015, ApJ, 806, 101. doi:10.1088/0004-637X/806/1/101
Hashemizadeh A., Driver S. P., Davies L. J. M., Robotham A. S. G., Bellstedt S., Windhorst R. A., Bremer M., et al., 2021, MNRAS, 505, 136. doi:10.1093/mnras/stab600
Hashemizadeh A., Driver S. P., Davies L. J. M., Robotham A. S. G., Bellstedt S., Foster C., Holwerda B. W., et al., 2022, MNRAS, 515, 1175. doi:10.1093/mnras/stac1195
Hasinger G., Capak P., Salvato M., Barger A. J., Cowie L. L., Faisst A., Hemmati S., et al., 2018, ApJ, 858, 77. doi:10.3847/1538-4357/aabacf
Heywood I., Jarvis M. J., Hale C. L., Whittam I. H., Bester H. L., Hugo B., Kenyon J. S., et al., 2022, MNRAS, 509, 2150. doi:10.1093/mnras/stab3021
Ilbert O., Arnouts S., McCracken H. J., Bolzonella M., Bertin E., Le Fèvre O., Mellier Y., et al., 2006, A&A, 457, 841. doi:10.1051/0004-6361:20065138
Jarvis M. J., et al., 2013, MNRAS, 428, 1281
Jarvis M., Taylor R., Agudo I., Allison J. R., Deane R. P., Frank B., Gupta N., et al., 2016, mks..conf, 6. doi:10.22323/1.277.0006
Jin S., Trager S. C., Dalton G. B., Aguerri J. A. L., Drew J. E., Falcón-Barroso J., Gänsicke B. T., et al., 2024, MNRAS, 530, 2688. doi:10.1093/mnras/stad557
de Jong R. S., Agertz O., Berbel A. A., Aird J., Alexander D. A., Amarsi A., Anders F., et al., 2019, Msngr, 175, 3. doi:10.18727/0722-6691/5117
Kafle P. R., Robotham A. S. G., Driver S. P., Deeley S., Norberg P., Drinkwater M. J., Davies L. J., 2018, arXiv, arXiv:1802.09009
Kauffmann G., Heckman T. M., White S. D. M., Charlot S., Tremonti C., Brinchmann J., Bruzual G., et al., 2003, MNRAS, 341, 33. doi:10.1046/j.1365-8711.2003.06291.x
Kauffmann G., Heckman T. M., Tremonti C., Brinchmann J., Charlot S., White S. D. M., Ridgway S. E., et al., 2003, MNRAS, 346, 1055. doi:10.1111/j.1365-2966.2003.07154.x
Kauffmann, G., White, S. D. M., Heckman, T. M., et al. 2004, MNRAS, 353, 713
Kelvin L. S., Driver S. P., Robotham A. S. G., Hill D. T., Alpaslan M., Baldry I. K., Bamford S. P., et al., 2012, MNRAS, 421, 1007. doi:10.1111/j.1365-2966.2012.20355.x
Khostovan A. A., Kartaltepe J. S., Salvato M., Ilbert O., Casey C. M., Algera H., Antwi-Danso J., et al., 2025, arXiv, arXiv:2503.00120. doi:10.48550/arXiv.2503.00120
Knobel C., Lilly S. J., Woo J., Kovač K., 2015, ApJ, 800, 24. doi:10.1088/0004-637X/800/1/24
Koushan S., Driver S. P., Bellstedt S., Davies L. J., Robotham A. S. G., Lagos C. del P., Hashemizadeh A., et al., 2021, MNRAS, 503, 2033. doi:10.1093/mnras/stab540
Kriek M., Shapley A. E., Reddy N. A., Siana B., Coil A. L., Mobasher B., Freeman W. R., et al., 2015, ApJS, 218, 15. doi:10.1088/0067-0049/218/2/15
Lagos C. del P., Bravo M., Tobar R., Obreschkow D., Power C., Robotham A. S. G., Proctor K. L., et al., 2024, MNRAS, 531, 3551. doi:10.1093/mnras/stae1024
Laigle C., et al., 2016, ApJS, 224, 24
Lange R., Driver S. P., Robotham A. S. G., Kelvin L. S., Graham A. W., Alpaslan M., Andrews S. K., et al., 2015, MNRAS, 447, 2603. doi:10.1093/mnras/stu2467
Larson R. B., Tinsley B. M., Caldwell C. N., 1980, ApJ, 237, 692
Lee K.-G., Krolewski A., White M., Schlegel D., Nugent P. E., Hennawi J. F., Müller T., et al., 2018, ApJS, 237, 31. doi:10.3847/1538-4365/aace58
Le Fèvre O., et al., 2013, A&A, 559, A14
Le Fèvre O., et al., 2014, Msngr, 155, 37
Le Fèvre O., Tasca L. A. M., Cassata P., Garilli B., Le Brun V., Maccagni D., Pentericci L., et al., 2015, A&A, 576, A79. doi:10.1051/0004-6361/201423829
Lewis, I. J., Cannon, R. D., Taylor, K., et al. 2002, MNRAS, 333, 279
Lewis I., Balogh M., De Propris R., Couch W., Bower R., Offer A., Bland-Hawthorn J., et al., 2002, MNRAS, 334, 673. doi:10.1046/j.1365-8711.2002.05558.x
Lilly S. J., et al., 2007, ApJS, 172, 70
Liske J., Baldry I. K., Driver S. P., Tuffs R. J., Alpaslan M., Andrae E., Brough S., et al., 2015, MNRAS, 452, 2087. doi:10.1093/mnras/stv1436
Mainieri V., Anderson R. I., Brinchmann J., Cimatti A., Ellis R. S., Hill V., Kneib J.-P., et al., 2024, arXiv, arXiv:2403.05398. doi:10.48550/arXiv.2403.05398
Mao Z., Kodama T., Pérez-Martínez J. M., Suzuki T. L., Yamamoto N.,

Adachi K., 2022, A&A, 666, A141. doi:10.1051/0004-6361/202243733
Martin, D. C., Wyder, T. K., Schiminovich, D., et al. 2007, ApJS, 173, 342
Masters D., Capak P., 2011, PASP, 123, 638. doi:10.1086/660023
Masters D. C., Stern D. K., Cohen J. G., Capak P. L., Stanford S. A., Hernitschek N., Galametz A., et al., 2019, ApJ, 877, 81. doi:10.3847/1538-4357/ab184d
McCracken H. J., et al., 2012, A&A, 544, A156
McGee S. L., Bower R. G., Balogh M. L., 2014, MNRAS, 442, L105. doi:10.1093/mnrasl/slu066
Momcheva I. G., Brammer G. B., van Dokkum P. G., Skelton R. E., Whitaker K. E., Nelson E. J., Fumagalli M., et al., 2016, ApJS, 225, 27. doi:10.3847/0067-0049/225/2/27
Moore, B., Katz, N., Lake, G., Dressler, A., & Oemler, A. 1996, Nature, 379, 613
Moore B., Lake G., Quinn T., Stadel J., 1999, MNRAS, 304, 465
Muzzin A., van der Burg R. F. J., McGee S. L., Balogh M., Franx M., Hoekstra H., Hudson M. J., et al., 2014, ApJ, 796, 65. doi:10.1088/0004-637X/796/1/65
Newman J. A., Cooper M. C., Davis M., Faber S. M., Coil A. L., Guhathakurta P., Koo D. C., et al., 2013, ApJS, 208, 5. doi:10.1088/0067-0049/208/1/5
Nichols, M., & Bland-Hawthorn, J. 2011, ApJ, 732, 17
Oxland M., Parker L. C., de Carvalho R. R., Sampaio V. M., 2024, MNRAS, 529, 3651. doi:10.1093/mnras/stae747
Patton D. R., Ellison S. L., Simard L., McConnachie A. W., Mendel J. T., 2011, MNRAS, 412, 591. doi:10.1111/j.1365-2966.2010.17932.x
Paulino-Afonso A., Sobral D., Darvish B., Ribeiro B., Stroe A., Best P., Afonso J., et al., 2018, A&A, 620, A186. doi:10.1051/0004-6361/201832688
Patton D. R., Ellison S. L., Simard L., McConnachie A. W., Mendel J. T., 2011, MNRAS, 412, 591. doi:10.1111/j.1365-2966.2010.17932.x
Peacock J. A., Cole S., Norberg P., Baugh C. M., Bland-Hawthorn J., Bridges T., Cannon R. D., et al., 2001, Natur, 410, 169. doi:10.1038/35065528
Peng Y.-. jie ., Lilly S. J., Kovač K., Bolzonella M., Pozzetti L., Renzini A., Zamorani G., et al., 2010, ApJ, 721, 193. doi:10.1088/0004-637X/721/1/193
Peng, Y.-j., Lilly, S. J., Renzini, A., & Carollo, M. 2012, ApJ, 757, 4
Peng, Y., Maiolino, R., & Cochrane, R. 2015, Nature, 521, 192
Pfeffer J., Cavanagh M. K., Bekki K., Couch W. J., Drinkwater M. J., Forbes D. A., Koribalski B. S., 2023, MNRAS, 518, 5260. doi:10.1093/mnras/stac3466
Poggianti B. M., et al., 2017, ApJ, 844, 48
Robotham A., Driver S. P., Norberg P., Baldry I. K., Bamford S. P., Hopkins A. M., Liske J., et al., 2010, PASA, 27, 76. doi:10.1071/AS09053
Robotham A. S. G., Norberg P., Driver S. P., Baldry I. K., Bamford S. P., Hopkins A. M., Liske J., et al., 2011, MNRAS, 416, 2640. doi:10.1111/j.1365-2966.2011.19217.x
Robotham A. S. G., et al., 2014, MNRAS, 444, 3986
Robotham A. S. G., Taranu D. S., Tobar R., Moffett A., Driver S. P., 2017, MNRAS, 466, 1513. doi:10.1093/mnras/stw3039
Robotham A. S. G., Davies L. J. M., Driver S. P., Koushan S., Taranu D. S., Casura S., Liske J., 2018, MNRAS, 476, 3137. doi:10.1093/mnras/sty440
Robotham A. S. G., Bellstedt S., Lagos C. del P., Thorne J. E., Davies L. J., Driver S. P., Bravo M., 2020, MNRAS, 495, 905. doi:10.1093/mnras/staa1116
Robotham A. S. G., Bellstedt S., Driver S. P., 2022, MNRAS, 513, 2985. doi:10.1093/mnras/stac1032
Paulino-Afonso A., Sobral D., Darvish B., Ribeiro B., Stroe A., Best P., Afonso J., et al., 2018, A&A, 620, A186. doi:10.1051/0004-6361/201832688
Saunders, W., Bridges, T., Gillingham, P., et al. 2004, Proc. SPIE, 5492, 389
Schaefer, A. L., Croom, S. M., Allen, J. T., et al. 2017, MNRAS, 464, 121
Scoville N., Aussel H., Brusa M., Capak P., Carollo C. M., Elvis M., Giavalisco M., et al., 2007, ApJS, 172, 1. doi:10.1086/516585
Sharp, R., Saunders, W., Smith, G., et al. 2006, Proc. SPIE, 6269, 62690G
Silverman J. D., Kashino D., Sanders D., Kartaltepe J. S., Arimoto N., Renzini A., Rodighiero G., et al., 2015, ApJS, 220, 12. doi:10.1088/0067-0049/220/1/12
Siudek M., Małek K., Pollo A., Iovino A., Haines C. P., Bolzonella M., Cucciati O., et al., 2022, A&A, 666, A131. doi:10.1051/0004-6361/202243613
Taylor E. N., Hopkins A. M., Baldry I. K., Brown M. J. I., Driver S. P., Kelvin L. S., Hill D. T., et al., 2011, MNRAS, 418, 1587. doi:10.1111/j.1365-2966.2011.19536.x
Taylor, E. N., Hopkins, A. M., Baldry, I. K., et al. 2015, MNRAS, 446, 2144
Tempel E., Stoica R. S., Martínez V. J., Liivamägi L. J., Castellan G., Saar E., 2014, MNRAS, 438, 3465. doi:10.1093/mnras/stt2454
Tempel E., Tamm A., Gramann M., Tuvikene T., Liivamägi L. J., Suhhonenko I., Kipper R., et al., 2014, A&A, 566, A1. doi:10.1051/0004-6361/201423585
Tempel E., Tuvikene T., Kipper R., Libeskind N. I., 2017, A&A, 602, A100. doi:10.1051/0004-6361/201730499
Thorne J. E., Robotham A. S. G., Davies L. J. M., Bellstedt S., Driver S. P., Bravo M., Bremer M. N., et al., 2021, MNRAS, 505, 540. doi:10.1093/mnras/stab1294
Thorne J. E., Robotham A. S. G., Davies L. J. M., Bellstedt S., Brown M. J. I., Croom S. M., Delvecchio I., et al., 2022, MNRAS, 509, 4940. doi:10.1093/mnras/stab3208
Tremonti C. A., Heckman T. M., Kauffmann G., Brinchmann J., Charlot S., White S. D. M., Seibert M., et al., 2004, ApJ, 613, 898. doi:10.1086/423264
Turner S., Siudek M., Salim S., Baldry I. K., Pollo A., Longmore S. N., Malek K., et al., 2021, MNRAS, 503, 3010. doi:10.1093/mnras/stab653
van der Burg R. F. J., Rudnick G., Balogh M. L., Muzzin A., Lidman C., Old L. J., Shipley H., et al., 2020, A&A, 638, A112. doi:10.1051/0004-6361/202037754
van der Wel A., Bell E. F., Holden B. P., Skibba R. A., Rix H.-W., 2010, ApJ, 714, 1779. doi:10.1088/0004-637X/714/2/1779
van der Wel A., Noeske K., Bezanson R., Pacifici C., Gallazzi A., Franx M., Muñoz-Mateos J. C., et al., 2016, ApJS, 223, 29. doi:10.3847/0067-0049/223/2/29
Weaver J. R., Kauffmann O. B., Ilbert O., McCracken H. J., Moneti A., Toft S., Brammer G., et al., 2022, ApJS, 258, 11. doi:10.3847/1538-4365/ac3078
Wetzel A. R., Tinker J. L., Conroy C., van den Bosch F. C., 2013, MNRAS, 432, 336. doi:10.1093/mnras/stt469
Wright A. H., Robotham A. S. G., Driver S. P., Alpaslan M., Andrews S. K., Baldry I. K., Bland-Hawthorn J., et al., 2017, MNRAS, 470, 283. doi:10.1093/mnras/stx1149
Yang X., Mo H. J., van den Bosch F. C., Pasquali A., Li C., Barden M., 2007, ApJ, 671, 153. doi:10.1086/522027

APPENDIX A: DR1 TABLE DESCRIPTIONS

In this appendix we detail the columns provided in the DR1 data release catalogues.

This paper has been typeset from a TEX/LATEX file prepared by the author.

Table A1. Additional columns in the `devils_dr1.D10ProFoundPhotometry` catalogue (which are not in Table 2). **Note:** all photometry measurements are provided for *total* flux measurements (no suffix) and colour-optimised flux measurements (suffix *_c) - see Davies et al. (2021) for details.

Name	Description	UCD	Unit	Type
NewSegID	Segment ID derived from segmentation maps - unique over full DEVILS region	meta.id		integer
field	DEVILS Field identifier (D02/D03/D10)	meta.id		character
R50_Y	The segment radius contain 50% of the VISTA Y-band flux	phys.angSize;em.IR.Y	arcsec	double
N100_Y	Number of segment pixels in the VISTA Y-band	phys.area		integer
subFrame	ProFound processing subFrame within the field that the segment is taken from	meta.id		integer
segIDFrame	Segment ID within subFrame (non-unique across DEVILS region)	meta.id		integer
xcenFrame	x position of the centre of the segment within the subFrame in the VISTA Y-band image	instr.pixel	pixel	double
ycenFrame	y position of the centre of the segment within the subFrame in the VISTA Y-band image	instr.pixel	pixel	double
xmaxFrame	x position of the brightest pixel of the segment within the subFrame in the VISTA Y-band image	instr.pixel	pixel	double
ymaxFrame	y position of the brightest pixel of the segment within the subFrame in the VISTA Y-band image	instr.pixel	pixel	double
EBV	Galactic Extinction correction coefficient applied to photometry - derived from Planck 2018 maps	phys.excitParam		double
flux_FUV	Total flux measured in GALEX FUV band	phot.flux.density;em.UV.100-200nm	Jy	double
flux_err_FUV	Error on total flux measured in GALEX FUV band	stat.error;phot.flux.density;em.UV.100-200nm	Jy	double
flux_NUV	Total flux measured in GALEX NUV band	phot.flux.density;em.UV.200-300nm	Jy	double
flux_err_NUV	Error on total flux measured in GALEX NUV band	stat.error;phot.flux.density;em.UV.200-300nm	Jy	double
flux_u	Total flux measured in CFHT-Megaprime u band	phot.flux.density;em.opt.u	Jy	double
flux_err_u	Error on total flux measured in CFHT-Megaprime u band	stat.error;phot.flux.density;em.opt.u	Jy	double
flux_g	Total flux measured in Subaru-HSC g band	phot.flux.density;em.opt.g	Jy	double
flux_err_g	Error on total flux measured in Subaru-HSC g band	stat.error;phot.flux.density;em.opt.g	Jy	double
flux_r	Total flux measured in Subaru-HSC r band	phot.flux.density;em.opt.r	Jy	double
flux_err_r	Error on total flux measured in Subaru-HSC r band	stat.error;phot.flux.density;em.opt.r	Jy	double
flux_i	Total flux measured in Subaru-HSC i band	phot.flux.density;em.opt.i	Jy	double
flux_err_i	Error on total flux measured in Subaru-HSC i band	stat.error;phot.flux.density;em.opt.i	Jy	double
flux_z	Total flux measured in Subaru-HSC z band	phot.flux.density;em.opt.z	Jy	double
flux_err_z	Error on total flux measured in Subaru-HSC z band	stat.error;phot.flux.density;em.opt.z	Jy	double
flux_HY	Total flux measured in Subaru-HSC Y band	phot.flux.density;em.IR.Y	Jy	double
flux_err_HY	Error on total flux measured in Subaru-HSC Y band	stat.error;phot.flux.density;em.IR.Y	Jy	double
flux_Y	Total flux measured in VISTA-VIRCAM Y band	phot.flux.density;em.IR.Y	Jy	double
flux_err_Y	Error on total flux measured in VISTA-VIRCAM Y band	stat.error;phot.flux.density;em.IR.Y	Jy	double
flux_J	Total flux measured in VISTA-VIRCAM J band	phot.flux.density;em.IR.J	Jy	double
flux_err_J	Error on total flux measured in VISTA-VIRCAM J band	stat.error;phot.flux.density;em.IR.J	Jy	double
flux_H	Total flux measured in VISTA-VIRCAM H band	phot.flux.density;em.IR.H	Jy	double
flux_err_H	Error on total flux measured in VISTA-VIRCAM H band	stat.error;phot.flux.density;em.IR.H	Jy	double
flux_Ks	Total flux measured in VISTA-VIRCAM Ks band	phot.flux.density;em.IR.Ks	Jy	double
flux_err_Ks	Error on total flux measured in VISTA-VIRCAM Ks band	stat.error;phot.flux.density;em.IR.Ks	Jy	double
flux_S36	Total flux measured in Spitzer-IRAC 3.6micron band	phot.flux.density;em.IR.3-4um	Jy	double
flux_err_S36	Error on total flux measured in Spitzer-IRAC 3.6micron band	stat.error;phot.flux.density;em.IR.3-4um	Jy	double
flux_S45	Total flux measured in Spitzer-IRAC 4.5micron band	phot.flux.density;em.IR.4-8um	Jy	double
flux_err_S45	Error on total flux measured in Spitzer-IRAC 4.5micron band	stat.error;phot.flux.density;em.IR.4-8um	Jy	double
flux_S58	Total flux measured in Spitzer-IRAC 5.8micron band	phot.flux.density;em.IR.4-8um	Jy	double
flux_err_S58	Error on total flux measured in Spitzer-IRAC 5.8micron band	stat.error;phot.flux.density;em.IR.4-8um	Jy	double
flux_S80	Total flux measured in Spitzer-IRAC 8.0micron band	phot.flux.density;em.IR.4-8um	Jy	double
flux_err_S80	Error on total flux measured in Spitzer-IRAC 8.0micron band	stat.error;phot.flux.density;em.IR.4-8um	Jy	double
flux_M24	Total flux measured in Spitzer-MIPS 24micron band	phot.flux.density;em.IR.15-30um	Jy	double
flux_err_M24	Error on total flux measured in Spitzer-MIPS 24micron band	stat.error;phot.flux.density;em.IR.15-30um	Jy	double
flux_M70	Total flux measured in Spitzer-MIPS 70micron band	phot.flux.density;em.IR.60-100um	Jy	double
flux_err_M70	Error on total flux measured in Spitzer-MIPS 70micron band	stat.error;phot.flux.density;em.IR.60-100um	Jy	double
flux_P100	Total flux measured in Herschel-PACS 100micron band	phot.flux.density;em.IR.FIR	Jy	double
flux_err_P100	Error on total flux measured in Herschel-PACS 100micron band	stat.error;phot.flux.density;em.IR.FIR	Jy	double
flux_P160	Total flux measured in Herschel-PACS 160micron band	phot.flux.density;em.IR.FIR	Jy	double
flux_err_P160	Error on total flux measured in Herschel-PACS 160micron band	stat.error;phot.flux.density;em.IR.FIR	Jy	double
flux_S250	Total flux measured in Herschel-SPIRE 250micron band	phot.flux.density;em.IR.FIR	Jy	double
flux_err_S250	Error on total flux measured in Herschel-SPIRE 250micron band	stat.error;phot.flux.density;em.IR.FIR	Jy	double
flux_S350	Total flux measured in Herschel-SPIRE 350micron band	phot.flux.density;em.IR.FIR	Jy	double
flux_err_S350	Error on total flux measured in Herschel-SPIRE 350micron band	stat.error;phot.flux.density;em.IR.FIR	Jy	double
flux_S500	Total flux measured in Herschel-SPIRE 500micron band	phot.flux.density;em.IR.FIR	Jy	double
flux_err_S500	Error on total flux measured in Herschel-SPIRE 500micron band	stat.error;phot.flux.density;em.IR.FIR	Jy	double

Table A2. Additional columns in the `devils_dr1.D10MasterRedshifts` catalogue (which are not in Table 2). Continued in Table A3

Name	Description	UCD	Unit	Type
DEVILS_ID	DEVILS spectroscopic ID taken from DEVILS-internal DMCat (DMCat2022-01-20)	meta.id		character
DEVILS_RA	DEVILS spectroscopic RA taken from DEVILS-internal DMCat (DMCat2022-01-20)	pos.eq.ra	deg	double
DEVILS_DEC	DEVILS spectroscopic DEC taken from DEVILS-internal DMCat (DMCat2022-01-20)	pos.eq.dec	deg	double
DEVILS_z	DEVILS current best spectroscopic redshift taken from DEVILS-internal DMCat (DMCat2022-01-20)	src.redshift		double
DEVILS_prob	DEVILS current best spectroscopic redshift probability (0-1) taken from DMCat (DMCat2022-01-20)	stat.probability;src.redshift		double
DEVILS_zPlus	DEVILS spectroscopic redshifts weighted by matches existing redshift information	src.redshift		double
DEVILS_probPlus	DEVILS weighted probability. DEVILS_prob +1 (if consistent with photo-z), +2 (if consistent with grism redshift), + 4 (if consistent with spec redshift). Numbers are adaptive, such that 7.xxx means redshift is consistent with existing photo-z, grism-z and spec-z	stat.probability;src.redshift		double
DEVILS_type	DEVILS redshift type	meta.id		character
zCOSMOS_ID	zCOSMOS spectroscopic ID taken from zCOSMOS Bright DR3 catalogue (zcosbrightspec20k_dr3_catalog_1595990782.csv - Lilly et al. (2007))	meta.id		character
zCOSMOS_RA	zCOSMOS spectroscopic RA taken from zCOSMOS Bright DR3 catalogue (zcosbrightspec20k_dr3_catalog_1595990782.csv)	pos.eq.ra	deg	double
zCOSMOS_DEC	zCOSMOS spectroscopic DEC taken from zCOSMOS Bright DR3 catalogue (zcosbrightspec20k_dr3_catalog_1595990782.csv)	pos.eq.dec	deg	double
zCOSMOS_z	zCOSMOS spectroscopic redshift taken from zCOSMOS Bright DR3 catalogue (zcosbrightspec20k_dr3_catalog_1595990782.csv)	src.redshift		double
zCOSMOS_prob	zCOSMOS spectroscopic confidence taken from zCOSMOS Bright DR3 catalogue (zcosbrightspec20k_dr3_catalog_1595990782.csv). 4=very secure, 3=secure, 2=probable, 1=insecure, 9=single line, 18=single line BL AGN....	meta.id		double
zCOSMOS_type	zCOSMOS redshift type	meta.id		character
DESI_ID	DESI spectroscopic ID taken from DESI EDR catalogue (zall-pix-edr-vac.fits - DESI Collaboration et al. (2024))	meta.id		character
DESI_RA	DESI spectroscopic RA taken from DESI EDR catalogue (zall-pix-edr-vac.fits)	pos.eq.ra	deg	double
DESI_DEC	DESI spectroscopic DEC taken from DESI EDR catalogue (zall-pix-edr-vac.fits)	pos.eq.dec	deg	double
DESI_z	DESI spectroscopic redshift taken from DESI EDR catalogue (zall-pix-edr-vac.fits)	src.redshift		double
DESI_prob	DESI spectroscopic confidence taken from DELTACHI2 in the DESI EDR catalogue (zall-pix-edr-vac.fits).Values >9 are classed as secure.	meta.id		double
DESI_type	DESI redshift type	meta.id		character
hCOSMOS_ID	hCOSMOS spectroscopic ID generated for hCOSMOS catalogue (a sequence using row order from hcosmosNew.cat.txt - Damjanov et al. (2018))	meta.id		character
hCOSMOS_RA	hCOSMOS spectroscopic RA taken from hCOSMOS catalogue (hcosmosNew.cat.txt)	pos.eq.ra	deg	double
hCOSMOS_DEC	hCOSMOS spectroscopic DEC taken from hCOSMOS catalogue (hcosmosNew.cat.txt)	pos.eq.dec	deg	double
hCOSMOS_z	hCOSMOS spectroscopic redshift taken from hCOSMOS catalogue (hcosmosNew.cat.txt)	src.redshift		double
hCOSMOS_prob	hCOSMOS spectroscopic error taken from hCOSMOS catalogue (hcosmosNew.cat.txt). Actual Δz.	stat.error;src.redshift		double
hCOSMOS_type	hCOSMOS redshift type	meta.id		character
DEIMOS_ID	DEIMOS spectroscopic ID taken from DEIMOS catalogue COSMOS_DEIMOS.csv - Hasinger et al. (2018))	meta.id		character
DEIMOS_RA	DEIMOS spectroscopic RA taken from DEIMOS catalogue (COSMOS_DEIMOS.csv)	pos.eq.ra	deg	double
DEIMOS_DEC	DEIMOS spectroscopic DEC taken from DEIMOS catalogue (COSMOS_DEIMOS.csv)	pos.eq.dec	deg	double
DEIMOS_z	DEIMOS spectroscopic redshift taken from DEIMOS catalogue (COSMOS_DEIMOS.csv)	src.redshift		double
DEIMOS_prob	DEIMOS spectroscopic quality flag taken from DEIMOS catalogue (COSMOS_DEIMOS.csv). 2=Reliable, 1.5=uncertain but agrees with photo-z, 1=uncertain	meta.id		double
DEIMOS_type	DEIMOS redshift type	meta.id		character
ComparatOII_ID	ComparatOII spectroscopic ID generated from ComparatOII catalogue (Comparat_catalog.dat - Comparat et al. (2015))	meta.id		character
ComparatOII_RA	ComparatOII spectroscopic RA taken from ComparatOII catalogue (Comparat_catalog.dat)	pos.eq.ra	deg	double
ComparatOII_DEC	ComparatOII spectroscopic DEC taken from ComparatOII catalogue (Comparat_catalog.dat)	pos.eq.dec	deg	double
ComparatOII_z	ComparatOII OII-derived spectroscopic Redshift taken from ComparatOII catalogue (Comparat_catalog.dat)	src.redshift		double
ComparatOII_prob	**NOTE** ComparatOII catalogue does not contain quality flags, added here to match data structure of other surveys	meta.id		double
ComparatOII_type	ComparatOII redshift type	meta.id		character
FMOS_ID	FMOS spectroscopic ID taken from FMOS catalogue FMOS_COSMOS_v1.0.fits - Silverman et al. (2015))	meta.id		character
FMOS_RA	FMOS spectroscopic RA taken from FMOS catalogue (FMOS_COSMOS_v1.0.fit)	pos.eq.ra	deg	double
FMOS_DEC	FMOS spectroscopic DEC taken from FMOS catalogue (FMOS_COSMOS_v1.0.fit)	pos.eq.dec	deg	double
FMOS_z	FMOS spectroscopic redshift taken from FMOS catalogue (FMOS_COSMOS_v1.0.fit)	src.redshift		double
FMOS_prob	FMOS spectroscopic quality flag taken from FMOS catalogue (FMOS_COSMOS_v1.0.fit). 4=Very secure, 3=secure, 2=probable, 1=not secure, 0=nothing	meta.id		double
FMOS_type	FMOS redshift type	meta.id		character
MOSDEF_ID	MOSDEF spectroscopic ID (ID_V4) taken from MOSDEF catalogue mosdef_zcat.final.fits - Kriek et al. (2015))	meta.id		character
MOSDEF_RA	MOSDEF spectroscopic RA taken from MOSDEF catalogue (mosdef_zcat.final.fits)	pos.eq.ra	deg	double
MOSDEF_DEC	MOSDEF spectroscopic DEC taken from MOSDEF catalogue (mosdef_zcat.final.fits)	pos.eq.dec	deg	double
MOSDEF_z	MOSDEF spectroscopic redshift taken from MOSDEF catalogue (mosdef_zcat.final.fits)	src.redshift		double
MOSDEF_prob	MOSDEF spectroscopic quality flag taken from MOSDEF catalogue (mosdef_zcat.final.fits)	meta.id		double
MOSDEF_type	MOSDEF redshift type	meta.id		character
C3R2_ID	C3R2 spectroscopic ID taken from C3R2 catalogue c3r2_DR1+DR2_2019april11.txt - Masters et al. (2019))	meta.id		character
C3R2_RA	C3R2 spectroscopic RA taken from C3R2 catalogue (c3r2_DR1+DR2_2019april11.txt)	pos.eq.ra	deg	double
C3R2_DEC	C3R2 spectroscopic DEC taken from C3R2 catalogue (c3r2_DR1+DR2_2019april11.txt)	pos.eq.dec	deg	double
C3R2_z	C3R2 spectroscopic redshift taken from C3R2 catalogue (c3r2_DR1+DR2_2019april11.txt)	src.redshift		double
C3R2_prob	C3R2 spectroscopic quality flag taken from C3R2 catalogue (c3r2_DR1+DR2_2019april11.txt). 4=certain, 3.5=very high confidence, 3=high confidence	meta.id		double
C3R2_type	C3R2 redshift type	meta.id		character
LRIS_ID	LRIS spectroscopic ID taken from LRIS catalogue cl2017_valueadded_release_20171009.txt - Lee et al. (2018))	meta.id		character
LRIS_RA	LRIS spectroscopic RA taken from LRIS catalogue (cl2017_valueadded_release_20171009.txt)	pos.eq.ra	deg	double
LRIS_DEC	LRIS spectroscopic DEC taken from LRIS catalogue (cl2017_valueadded_release_20171009.txt)	pos.eq.dec	deg	double
LRIS_z	LRIS spectroscopic redshift taken from LRIS catalogue (cl2017_valueadded_release_20171009.txt)	src.redshift		double
LRIS_prob	LRIS spectroscopic quality flag taken from LRIS catalogue (cl2017_valueadded_release_20171009.txt). 4=high confidence, 3=reasonable confidence, 2=low-confidence, 1=guess	meta.id		double
LRIS_type	LRIS redshift type	meta.id		character
VIS3COSMOS_ID	VIS3COSMOS spectroscopic ID taken from VIS3COSMOS catalogue VIS3COSMOS_tableb1.dat - Paulino-Afonso et al. (2018))	meta.id		character
VIS3COSMOS_RA	VIS3COSMOS spectroscopic RA taken from VIS3COSMOS catalogue (VIS3COSMOS_tableb1.dat)	pos.eq.ra	deg	double
VIS3COSMOS_DEC	VIS3COSMOS spectroscopic DEC taken from VIS3COSMOS catalogue (VIS3COSMOS_tableb1.dat)	pos.eq.dec	deg	double
VIS3COSMOS_z	VIS3COSMOS spectroscopic redshift taken from VIS3COSMOS catalogue (VIS3COSMOS_tableb1.dat)	src.redshift		double
VIS3COSMOS_prob	VIS3COSMOS catalogue (VIS3COSMOS_tableb1.dat) has no quality flag	meta.id		double
VIS3COSMOS_type	VIS3COSMOS redshift type	meta.id		character
LEGA_C_ID	LEGA_C spectroscopic ID taken from LEGA_C catalogue ADP.2018-06-13T13:17:01.234.fits - van der Wel et al. (2016))	meta.id		character
LEGA_C_RA	LEGA_C spectroscopic RA taken from LEGA_C catalogue (ADP.2018-06-13T13:17:01.234.fits)	pos.eq.ra	deg	double
LEGA_C_DEC	LEGA_C spectroscopic DEC taken from LEGA_C catalogue (ADP.2018-06-13T13:17:01.234.fits)	pos.eq.dec	deg	double
LEGA_C_z	LEGA_C spectroscopic redshift taken from LEGA_C catalogue (ADP.2018-06-13T13:17:01.234.fits)	src.redshift		double
LEGA_C_prob	LEGA_C catalogue redshift quality flag (ADP.2018-06-13T13:17:01.234.fits). 0=good redshift, 1=bad redshift	meta.id		double
LEGA_C_type	LEGA_C redshift type	meta.id		character

Table A3. Table A2 continued... Additional columns in the `devils_dr1.D10MasterRedshifts` catalogue (which are not in Table 2).

Name	Description	UCD	Unit	Type
VVDS_ID	VVDS spectroscopic ID taken from VVDS catalogue VVDS_COSMOS.csv - Le Fèvre et al. (2013))	meta.id		character
VVDS_RA	VVDS spectroscopic RA taken from VVDS catalogue (VVDS_COSMOS.csv)	pos.eq.ra	deg	double
VVDS_DEC	VVDS spectroscopic DEC taken from VVDS catalogue (VVDS_COSMOS.csv)	pos.eq.dec	deg	double
VVDS_z	VVDS spectroscopic redshift taken from VVDS catalogue (VVDS_COSMOS.csv)	src.redshift		double
VVDS_prob	VVDS spectroscopic quality flag taken from VVDS catalogue (VVDS_COSMOS.csv). 4=high confidence, 3=reasonable confidence, 2=low-confidence, 1=guess	meta.id		double
VVDS_type	VVDS redshift type	meta.id		character
VUDS_ID	VUDS spectroscopic ID taken from OzDES master catalogue OzDES_GRC_2017_08_30.csv - Le Fèvre et al. (2015))	meta.id		character
VUDS_RA	VUDS spectroscopic RA taken from VUDS catalogue (OzDES_GRC_2017_08_30.csv)	pos.eq.ra	deg	double
VUDS_DEC	VUDS spectroscopic DEC taken from VUDS catalogue (OzDES_GRC_2017_08_30.csv)	pos.eq.dec	deg	double
VUDS_z	VUDS spectroscopic redshift taken from VUDS catalogue (OzDES_GRC_2017_08_30.csv)	src.redshift		double
VUDS_prob	VUDS spectroscopic quality flag taken from VUDS catalogue (OzDES_GRC_2017_08_30.csv). reliable = 1.5,2,3,4,9	meta.id		double
VUDS_type	VUDS redshift type	meta.id		character
PRIMUS_ID	PRIMUS grism ID taken from PRIMUS catalogue PRIMUS_2013_zcat_v1.fits - Cool et al. (2013))	meta.id		character
PRIMUS_RA	PRIMUS grism RA taken from PRIMUS catalogue (PRIMUS_2013_zcat_v1.fits)	pos.eq.ra	deg	double
PRIMUS_DEC	PRIMUS grism DEC taken from PRIMUS catalogue (PRIMUS_2013_zcat_v1.fits)	pos.eq.dec	deg	double
PRIMUS_z	PRIMUS grism redshift taken from PRIMUS catalogue (PRIMUS_2013_zcat_v1.fits)	src.redshift		double
PRIMUS_prob	PRIMUS grism quality flag taken from PRIMUS catalogue (PRIMUS_2013_zcat_v1.fits). 44=high quality (dz/(1+z) 0.003), 3=good quality dz/(1+z) 0.015), 2=probable dz/(1+z) 0.03, -1=star	meta.id		double
PRIMUS_type	PRIMUS redshift type	meta.id		character
HST3D_ID	HST3D grism ID taken from HST3D catalogue cosmos_3dhst.v4.1.5.zbest.fits - Momcheva et al. (2016) - only use_zgrism=1	meta.id		character
HST3D_RA	HST3D grism RA taken from HST3D catalogue (cosmos_3dhst.v4.1.5.zbest.fits)	pos.eq.ra	deg	double
HST3D_DEC	HST3D grism DEC taken from HST3D catalogue (cosmos_3dhst.v4.1.5.zbest.fits)	pos.eq.dec	deg	double
HST3D_z	HST3D grism redshift taken from HST3D catalogue (cosmos_3dhst.v4.1.5.zbest.fits)	src.redshift		double
HST3D_l68	HST3D grism 1sigma lower confidence boundary taken from HST3D catalogue (cosmos_3dhst.v4.1.5.zbest.fits).	stat.error;src.redshift		double
HST3D_u68	HST3D grism 1sigma upper confidence boundary taken from HST3D catalogue (cosmos_3dhst.v4.1.5.zbest.fits).	stat.error;src.redshift		double
HST3D_type	HST3D redshift type	meta.id		character
PAU_ID	PAU PhotoZ ID taken from PAU catalogue pau_cosmos_photoz_v0_4_c.fits - Alarcon et al. (2021).	meta.id		character
PAU_RA	PAU PhotoZ RA taken from PAU catalogue (pau_cosmos_photoz_v0_4_c.fits)	pos.eq.ra	deg	double
PAU_DEC	PAU PhotoZ DEC taken from PAU catalogue (pau_cosmos_photoz_v0_4_c.fits)	pos.eq.dec	deg	double
PAU_z	PAU PhotoZ redshift taken from PAU catalogue (pau_cosmos_photoz_v0_4_c.fits)	src.redshift		double
PAU_l68	**NOTE** PAU PhotoZ catalogue has no error bound. Added here to match structure of other surveys	stat.error;src.redshift		double
PAU_u68	**NOTE** PAU PhotoZ catalogue has no error bound. Added here to match structure of other surveys	stat.error;src.redshift		double
PAU_type	PAU redshift type	meta.id		character
COSMOS2015_ID	COSMOS2015 PhotoZ ID (ID2013) taken from COSMOS2015 catalogue COSMOS2015_Laigle+_v1.1.fits - Laigle et al. (2016)	meta.id		character
COSMOS2015_RA	COSMOS2015 PhotoZ RA taken from COSMOS2015 catalogue (COSMOS2015_Laigle+_v1.1.fits)	pos.eq.ra	deg	double
COSMOS2015_DEC	COSMOS2015 PhotoZ DEC taken from COSMOS2015 catalogue (COSMOS2015_Laigle+_v1.1.fits)	pos.eq.dec	deg	double
COSMOS2015_z	COSMOS2015 PhotoZ (ZPDF) redshift taken from COSMOS2015 catalogue (COSMOS2015_Laigle+_v1.1.fits)	src.redshift		double
COSMOS2015_l68	COSMOS2015 PhotoZ 1sigma lower confidence boundary taken from COSMOS2015 catalogue (COSMOS2015_Laigle+_v1.1.fits).	stat.error;src.redshift		double
COSMOS2015_u68	COSMOS2015 PhotoZ 1sigma upper confidence boundary taken from COSMOS2015 catalogue (COSMOS2015_Laigle+_v1.1.fits).	stat.error;src.redshift		double
COSMOS2015_type	COSMOS2015 redshift type	meta.id		character
MIGHTEEtmp_ID	MIGHTEEtmp PhotoZ ID taken from MIGHTEEtmp catalogue COS_Master_hatfield_GPz_V1.fits - Adams et al. (2020)	meta.id		character
MIGHTEEtmp_RA	MIGHTEEtmp PhotoZ RA taken from MIGHTEEtmp catalogue (COS_Master_hatfield_GPz_V1.fits)	pos.eq.ra	deg	double
MIGHTEEtmp_DEC	MIGHTEEtmp PhotoZ DEC taken from MIGHTEEtmp catalogue (COS_Master_hatfield_GPz_V1.fits)	pos.eq.dec	deg	double
MIGHTEEtmp_z	MIGHTEEtmp PhotoZ (Z_GPz_all) redshift taken from MIGHTEEtmp catalogue (COS_Master_hatfield_GPz_V1.fits)	src.redshift		double
MIGHTEEtmp_l68	**NOTE** No error provided for MIGHTEEtmp PhotoZ. Added here to match structure of other surveys (COS_Master_hatfield_GPz_V1.fits).	stat.error;src.redshift		double
MIGHTEEtmp_u68	**NOTE** No error provided for MIGHTEEtmp PhotoZ. Added here to match structure of other surveys(COS_Master_hatfield_GPz_V1.fits).	stat.error;src.redshift		double
MIGHTEEtmp_type	MIGHTEEtmp redshift type	meta.id		character
zBest	Best Redshift for source from all available redshifts (see text for details)	src.redshift		double
zBestSource	Survey from which best redshift comes, identifier in column names	meta.id		character
zBestType	Type of redshift: spec, grism, photoz	meta.id		character

Table A4. Additional columns in the `devils_dr1.D10ProSpectNoAGN` catalogue (which are not in Table 2). **Note:** for all parameters in this table the catalogue also provides the 1σ upper and lower bounds of the MCMC chains with suffix *_UB and *_LB respectively.

Name	Description	UCD	Unit	Type
z	Redshift used in ProSpect SED fitting (can differ from `devils_dr1.D10MasterRedshifts`)	src.redshift		double
mSFR	ProSpect parameter that controls the maximum star formation rate in the skewed normal - logged	stat.param	log(solMass/yr)	double
mpeak	ProSpect parameter that controls where the peak of star formation occurs	stat.param	Gyr	double
mperiod	ProSpect parameter that controls the width of the star formation skewed Normal - logged	stat.param	log(Gyr)	double
mskew	ProSpect Parameter that controls the skew of the skewed Normal	stat.param		double
tau_birth	ProSpect parameter to describe the column density of dust in the birth clouds - logged	stat.param		double
tau_screen	ProSpect parameter to describe the column density of dust in the ISM- logged	stat.param		double
alpha_SF_birth	ProSpect parameter to describe the temperature of the dust in the birth clouds	stat.param		double
alpha_SF_screen	ProSpect parameter to describe the temperature of the dust in the ISM	stat.param		double
Zfinal	Final gas-phase metallicity, modelled in ProSpect - logged	stat.param;phys.abund.Z		double
LP	log-posterior of best fit model in ProSpect	stat.likelihood		double
StellarMass	Remaining galaxy stellar mass (assuming returned fraction), generally this should be the value to use for stellar masses	phys.mass	solMass	double
StellarMassFormed	Total stellar mass formed, not remaining (*i.e.* assuming no returned fraction)	phys.mass	solMass	double
dustmass.birth	Dust mass in birth clouds	phys.mass	solMass	double
dustmass.screen	Dust mass in ISM	phys.mass	solMass	double
dustmass.total	Dust mass total	phys.mass	solMass	double
dustlum.birth	Dust luminosity in birth clouds	phys.luminosity	solLum	double
dustlum.screen	Dust luminosity in ISM	phys.luminosity	solLum	double
dustlum.total	Dust luminosity total	phys.luminosity	solLum	double
SFRburst	SFR measured over 100Myr baseline, generally this should be the value uses for SFRs	phys.SFR	solMass/yr	double
flux.galex_fuv	best fit model flux in galex_fuv	phot.flux.density	Jy	double
flux.galex_nuv	best fit modelflux in galex_nuv	phot.flux.density	Jy	double
flux.cfht_u	best fit model flux in cfht_u	phot.flux.density	Jy	double
flux.hsc_g	best fit model flux in hsc_g	phot.flux.density	Jy	double
flux.hsc_r	best fit model flux in hsc_r	phot.flux.density	Jy	double
flux.hsc_i	best fit model flux in hsc_i	phot.flux.density	Jy	double
flux.hsc_z	best fit model flux in hsc_z	phot.flux.density	Jy	double
flux.vista_Y	best fit model flux in vista_Y	phot.flux.density	Jy	double
flux.vista_J	best fit model flux in vista_J	phot.flux.density	Jy	double
flux.vista_H	best fit model flux in vista_H	phot.flux.density	Jy	double
flux.vista_Ks	best fit model flux in vista_Ks	phot.flux.density	Jy	double
flux.irac_1	best fit model flux in irac_1	phot.flux.density	Jy	double
flux.irac_2	best fit model flux in irac_2	phot.flux.density	Jy	double
flux.irac_3	best fit model flux in irac_3	phot.flux.density	Jy	double
flux.irac_4	best fit model flux in irac_4	phot.flux.density	Jy	double
flux.mips_24	best fit model flux in mips_24	phot.flux.density	Jy	double
flux.mips_70	best fit model flux in mips_70	phot.flux.density	Jy	double
flux.pacs_100	best fit model flux in pacs_100	phot.flux.density	Jy	double
flux.pacs_160	best fit model flux in pacs_160	phot.flux.density	Jy	double
flux.spire_250	best fit model flux in spire_250	phot.flux.density	Jy	double
flux.spire_350	best fit model flux in spire_350	phot.flux.density	Jy	double
flux.spire_500	best fit model flux in spire_500	phot.flux.density	Jy	double

Table A5. Additional cdditional columns in the `devils_dr1.D10ProSpectAGN` catalogue (which are not in Table 2 and are not already listed in Table A4). **Note:** for all parameters in this table the catalogue also provides the 1σ upper and lower bounds of the MCMC chains with suffix *_UB and *_LB respectively.

Name	Description	UCD	Unit	Type
AGNlum	Bolometric luminosity of AGN source - logged	phys.luminosity.bol;stat.min	log(erg/s)	double
AGNan	Angle of observation of AGN source	phys.ang;stat.min	deg	double
AGNta	Optical depth tau of AGN source - logged	phys.absorption.opticalDepth;stat.min		double
LP	Log posterior of best fit model in ProSpect	stat.likelihood;stat.min		double
AGNfrac	fraction of flux contributed by the AGN component between 5-20micron	phys.luminosity.bol;stat.weight		double
Type	AGN type 1 or 2	meta.code.class		integer
Iteration	Iteration for convergence	meta.number		integer
flux_3GHz	predicted flux at 3GHz from ProSpect fit	em.radio.3-6GHz;stat.value	Jy	double
HalfMassAge	The age taken to form half the galaxy's mass based on the best fit SFH	phys.age	Gyr	double

Table A6. Additional columns in the `devils_dr1.D10ProFitStructure` catalogue (which are not in Table 2).

Name	Description	UCD	Unit	Type
vis_morph	Visual morphology class from `devils_dr1.D10VisualMorphology` catalogue	src.morph.type		character
best_model	The preferred model based on the outputs of the model fit: twocomps, puredisk, spheroid, failed (see Cook et al. 2025)	meta.id		character
class	The preferred model based on the visual inspections and adjusted accordingly based on the best-fitting model parameters: twocomps, puredisk, spheroid, failed (see Cook et al. 2025)	meta.id		character
magBulge	Final Class: Bulge Profile integrated HST F814W magnitude	phot.mag;em.opt.I	mag	double
magDisk	Final Class: Disk Profile integrated HST F814W magnitude	phot.mag;em.opt.I	mag	double
reBulge_pix	Final Class: Bulge Observed effective radius (R50) in pixels	phys.size.radius;em.opt.I	pixel	double
reDisk_pix	Final Class: Disk Observed effective radius (R50) in pixels	phys.size.radius;em.opt.I	pixel	double
reTotal_pix	Final Class: Total (disk+bulge) Observed effective radius (R50) in pixels	phys.size.radius;em.opt.I	pixel	double
reBulge_kpc	Final Class: Bulge physical effective radius (R50) in kpc	phys.size.radius;em.opt.I	kpc	double
reDisk_kpc	Final Class: Disk physical effective radius (R50) in kpc	phys.size.radius;em.opt.I	kpc	double
reTotal_kpc	Final Class: Total (disk+bulge) Observed effective radius (R50) in kpc	phys.size.radius;em.opt.I	kpc	double
nserBulge	Final Class: Bulge Sersic Index	src.morph.type;em.opt.I		double
nserDisk	Final Class: Disk Sersic Index	src.morph.type;em.opt.I		double
axratBulge	Final Class: Bulge Axial Ratio	phys.size.axisRatio;em.opt.I		double
axratDisk	Final Class: Disk Axial Ratio	phys.size.axisRatio;em.opt.I		double
angBulge	Final Class: Bulge Position angle (increasing clockwise 0 deg from North)	pos.posAng;em.opt.I	deg	double
angDisk	Final Class: Disk Position angle (increasing clockwise 0 deg from North)	pos.posAng;em.opt.I	deg	double
B2T_corr	Final Class: Light-weighted Bulge-to-total ratio	src.morph.type		double
xcen_single	Single component fit: Central x pixel position	pos.centroid	pixel	double
ycen_single	Single component fit: Central y pixel position	pos.centroid	pixel	double
mag_single	Single component fit: Profile integrated HST F814W magnitude	phot.mag;em.opt.I	mag	double
re_single_kpc	Single component fit: Effective radius (R50) in kpc	phys.size.radius;em.opt.I	kpc	double
nser_single	Single component fit: Sersic Index	src.morph.type;em.opt.I		double
ang_single	Single component fit: Position angle (increasing clockwise 0 deg from North)	pos.posAng;em.opt.I	deg	double
axrat_single	Single component fit: Axial Ratio	phys.size.axisRatio;em.opt.I		double
xcen_err_single	Single component fit: Central x pixel position Error	stat.error;pos.centroid	pixel	double
ycen_err_single	Single component fit: Central y pixel position Error	stat.error;pos.centroid	pixel	double
mag_err_single	Single component fit: Profile integrated HST F814W magnitude Error	stat.error;phot.mag;em.opt.I	mag	double
re_err_single	Single component fit: Effective radius (R50) in kpc Error	stat.error;phys.size.radius;em.opt.I	kpc	double
nser_err_single	Single component fit: Sersic Index Error	stat.error;src.morph.type;em.opt.I		double
ang_err_single	Single component fit: Position angle (increasing clockwise 0 deg from North) Error	stat.error;pos.posAng;em.opt.I	deg	double
axrat_err_single	Single component fit: Axial Ratio Error	stat.error;phys.size.axisRatio;em.opt.I		double
LP_single	Single component fit: LP for best fit	stat.fit.goodness		double
DIC_single	Single component fit: deviance information criterion for best fit	stat.fit.goodness		double
time_single	Single component fit: time to run ProFuse fit	time.duration	sec	double
xcen_serexp	Sersic Bulge + Exponential Disk fit: Central x pixel position	pos.centroid	pixel	double
ycen_serexp	Sersic Bulge + Exponential Disk fit: Central y pixel position	pos.centroid	pixel	double
mag1_serexp	Sersic Bulge + Exponential Disk fit: Comp1 Profile integrated HST F814W magnitude	phot.mag;em.opt.I	mag	double
mag2_serexp	Sersic Bulge + Exponential Disk fit: Comp2 Profile integrated HST F814W magnitude	phot.mag;em.opt.I	mag	double
re1_serexp_kpc	Sersic Bulge + Exponential Disk fit: Comp1 Effective radius (R50) in kpc	phys.size.radius;em.opt.I	kpc	double
re2_serexp_kpc	Sersic Bulge + Exponential Disk fit: Comp2 effective radius (R50) in kpc	phys.size.radius;em.opt.I	kpc	double
nser1_serexp	Sersic Bulge + Exponential Disk fit: Comp1 Sersic Index	src.morph.type;em.opt.I		double
ang2_serexp	Sersic Bulge + Exponential Disk fit: Comp2 Position angle (increasing clockwise 0 deg from North)	pos.posAng;em.opt.I	deg	double
axrat2_serexp	Sersic Bulge + Exponential Disk fit: Comp2 Axial Ratio	phys.size.axisRatio;em.opt.I		double
xcen_err_serexp	Sersic Bulge + Exponential Disk fit: Central x pixel position Error	stat.error;pos.centroid	pixel	double
ycen_err_serexp	Sersic Bulge + Exponential Disk fit: Central y pixel position Error	stat.error;pos.centroid	pixel	double
mag1_err_serexp	Sersic Bulge + Exponential Disk fit: Comp1 Profile integrated HST F814W magnitude Error	stat.error;phot.mag;em.opt.I	mag	double
mag2_err_serexp	Sersic Bulge + Exponential Disk fit: Comp2 Profile integrated HST F814W magnitude Error	stat.error;phot.mag;em.opt.I	mag	double
re1_err_serexp	Sersic Comp1 + Exponential Disk fit: Comp1 Effective radius (R50) in kpc Error	stat.error;phys.size.radius;em.opt.I	kpc	double
re2_err_serexp	Sersic Bulge + Exponential Disk fit: Comp2 effective radius (R50) in kpc Error	stat.error;phys.size.radius;em.opt.I	kpc	double
nser1_err_serexp	Sersic Bulge + Exponential Disk fit: Comp1 Sersic Index Error	stat.error;src.morph.type;em.opt.I		double
ang2_err_serexp	Sersic Bulge + Exponential Disk fit: Comp2 Position angle (increasing clockwise 0 deg from North) Error	stat.error;pos.posAng;em.opt.I	deg	double
axrat2_err_serexp	Sersic Bulge + Exponential Disk fit: Comp2 Axial Ratio Error	stat.error;phys.size.axisRatio;em.opt.I		double
LP_serexp	Sersic Bulge + Exponential Disk fit: LP for best fit	stat.fit.goodness		double
DIC_serexp	Sersic Bulge + Exponential Disk fit: deviance information criterion for best fit	stat.fit.goodness		double
time_serexp	Sersic Bulge + Exponential Disk fit: time to run ProFuse fit	src.morph.type	sec	integer
B2T_serexp	Sersic Bulge + Exponential Disk fit: Light-weighted Comp1-to-Comp1+2 ratio	time.duration		integer
nexps	Number of HST exposures included in fit	stat.value		double
npixels	Number of HST pixels used in the profile fitting	instr.pixel		double

Table A7. Additional columns in the `devils_dr1.D10VisualMorphology` catalogue (which are not in Table 2). Note: some columns in this catalogue as replicated from other catalogues, and are superseded by the other base catalogue values. They are retained here as they were used in the selection of the visual morphological sample.

Name	Description	UCD	Unit	Type
ProSpect_Mstar	ProSpect stellar mass taken from Thorne et al. (2021) - used for sample selection	phys.mass.stars	log(solMass)	double
ProSpect_Mstar_LB	ProSpect stellar mass lower bound of final MCMC chain taken from Thorne et al. (2021) - used for sample selection	phys.mass.stars;stat.min	log(solMass)	double
ProSpect_Mstar_UB	ProSpect stellar mass upper bound of final MCMC chain taken from Thorne et al. (2021) - used for sample selection	phys.mass.stars;stat.max	log(solMass)	double
ProSpect_SFR	ProSpect burst SFR taken from Thorne et al. (2021) - used for sample selection	phys.sfr	log(solMass/yr)	double
ProSpect_SFR_LB	ProSpect burst SFR lower bound of final MCMC chain taken from Thorne et al. (2021) - used for sample selection	phys.sfr;stat.min	log(solMass/yr)	double
ProSpect_SFR_UB	ProSpect burst SFR upper bound of final MCMC chain taken from Thorne et al. (2021) - used for sample selection	phys.sfr;stat.max	log(solMass/yr)	double
DEVILS_ID	DEVILS spectroscopic ID from `devils_dr1.D10MasterRedshifts` catalogue	meta.id		character
Laigle_logMstar	Stellar mass measurement from the COSMOS2015 catalogue - used for sample selection	phys.mass.stars	log10(solMass)	double
G10_zBest	Best redshift from the Davies et al. (2015) G10/COSMOS catalogue	src.redshift		double
SERSIC_n_SINGLE	Sersic index from initial ProFit single component Sersic fit to HST F814W band	phys.size.sersic		double
AUTO_CLASS	Automatic morphology class from Galaxy Zoo and ANN combination	meta.id		character
FIRST_CLASS	First rough classification	meta.id		character
CHECKER	Second pass name of visual checker	meta.id		character
SPD_CLASS	Simon Driver visual classification	meta.id		character
SB_CLASS	Sabine Bellstedt visual classification	meta.id		character
LJMD_CLASS	Luke Davies visual classification	meta.id		character
FINAL_CLASS	Final visual classification based on combination of all classifiers	meta.id		character
HSTreg	Is galaxy within the useable HST-COSMOS region? 1=yes, 0=no	meta.id		integer
sampSel	Is galaxy within the DEVILS morphology sample selection 1=yes, 0=no (ProSpect_Mstar>$10^{9.5}$ & zBest<1.0 & RAcen>=149.5)?	meta.id		integer

Table A8. Additional columns in the `devils_dr1.D10GroupGals` catalogue (which are not in Table 2).

Name	Description	UCD	Unit	Type
apmag_Y	Apparent Y-band magnitude (AB).	phot.mag; em.IR.Y	mag	double
DM_737	Distance modulus assuming a 737 cosmology (h_0 = 0.7, Ω_m = 0.3, and Ω_Λ = 0.7).	phot.mag.distMod	mag	double
SigErr	Velocity uncertainty on redshift, assumed to be 45 km s^{-1} for all spectroscopic redshifts.	phys.veloc	km s^{-1}	double
GroupID	ID of the group the galaxy is member (value of 0 for isolated galaxies).	meta.id; meta.main		integer
RankIterCen	Relative ranking of galaxy by projected distance to the iteratively-calculated group centre. 1=closest galaxy (*i.e.*, central), n=n-th closest galaxy. -999 for isolated galaxies.	stat.rank		integer
SepIterCen	Projected angular separation of the galaxy to the RankIterCen = 1 galaxy.	phys.angSize	arcsec	double
CoSepIterCen	Projected comoving distance separation of the galaxy to the RankIterCen = 1 galaxy.	phys.size.radius	Mpc h^{-1}	double
AngSepIterCen	Projected angular size distance separation of the galaxy to the RankIterCen = 1 galaxy.	phys.size.radius	Mpc h^{-1}	double
RankBCG	Relative ranking of galaxy by projected distance to the BCG. 1=BCG in the group, 2=closest satellite, n=(n-1)-th closest galaxy. -999 for isolated galaxies.	stat.rank		integer
SepBCG	Projected angular separation of the galaxy to the BCG.	phys.angSize	arcsec	double
CoSepBCG	Projected comoving distance separation of the galaxy to the BCG.	phys.size.radius	Mpc h^{-1}	double
AngSepBCG	Projected angular size distance separation of the galaxy to the BCG.	phys.size.radius	Mpc h^{-1}	double
RankCen	1= closest galaxy to group centre, 2=closest satellite, n=n-th closest galaxy. -999 for isolated galaxies.	stat.rank		integer
SepCen	Projected angular separation of the galaxy to the group centre.	phys.angSize	arcsec	double
CoSepCen	Projected comoving distance separation of the galaxy to the group centre.	phys.size.radius	Mpc h^{-1}	double
AngSepCen	Projected angular size distance separation of the galaxy to the group centre.	phys.size.radius	Mpc h^{-1}	double

Table A9. Additional columns in the `devils_dr1.D10Groups` catalogue (which are not in Table 2).

Name	Description	UCD	Unit	Type
GroupID	Unique ID of the galaxy group.	meta.id; meta.main		integer
Nfof	Number of member galaxies.	stat.value		integer
Zfof	Median redshift of the group members.	src.redshift		double
IterCenUID	UID of the RankIterCen = 1 galaxy.	meta.id		integer
IterCenRA	Right ascension of the RankIterCen = 1 galaxy.	pos.eq.ra	deg	double
IterCenDEC	Declination of the RankIterCen = 1 galaxy.	pos.eq.dec	deg	double
IterCenZ	Redshift of the RankIterCen = 1 galaxy.	src.redshift		double
BCGUID	UID of the RankBCG = 1 galaxy.	meta.id		integer
BCGRA	Right ascension of the RankBCG = 1 galaxy.	pos.eq.ra	deg	double
BCGDEC	Declination of the RankBCG = 1 galaxy.	pos.eq.dec	deg	double
CenRA	Right ascension of centre of luminosity of the group.	pos.eq.ra	deg	double
CenDEC	Declination of centre of luminosity of the group.	pos.eq.dec	deg	double
Rad50	Radius of the smallest projected circle containing 50% of the group members, centred on the IterCenUID galaxy.	phys.size.radius	Mpc h^{-1}	double
Rad1Sig	Radius of the smallest projected circle containing 68% of the group members, centred on the IterCenUID galaxy.	phys.size.radius	Mpc h^{-1}	double
Rad100	Radius of the smallest projected circle containing 100% of the group members, centred on the IterCenUID galaxy.	phys.size.radius	Mpc h^{-1}	double
RelDen	Relative galaxy space density within a cylinder of radius 1.5 Mpc h^{-1} and length 24 Mpc h^{-1} centred on the IterCenUID galaxy, *i.e.*, ratio between measured density and expected density from the $N(z)$ fit in the cylinder.	src.density		double
GroupEdge	Fraction of the group within survey volume, estimated using IterCen and Rad100.			double
VelDispRaw	Raw measurement of the group velocity dispersion.	phys.veloc	km s^{-1}	double
VelErr	Total velocity error of the group.	phys.veloc	km s^{-1}	double
VelDisp	Group velocity dispersion, corrected for the total velocity measurement error. Set to 0 if total error is larger than the raw velocity (*i.e.*, VelErr>VelDisp).	phys.veloc	km s^{-1}	double
GroupMass	Dynamical group mass estimated using $M_{halo} \propto (Rad_{50} \times VelDisp^2)$. See section 4.3 of Robotham et al. (2011) for further details.	phys.mass	$M_\odot$ h^{-1}	double
GroupMassA	Dynamical group mass estimated using $M_{halo} \propto (Rad_{50} \times VelDisp^2)$, corrected for median biases by a scalar factor. See section 4.3 of Robotham et al. (2011) for further details.	phys.mass	$M_\odot$ h^{-1}	double
GroupMassAfunc	Dynamical group mass estimated using $M_{halo} \propto (Rad_{50} \times VelDisp^2)$, corrected for median biases by a function of both Nfof and IterCenZ. See section 4.3 of Robotham et al. (2011) for further details.	phys.mass	$M_\odot$ h^{-1}	double
LinkTot	Number of FoF links in the group.	stat.value		integer
LinkStrenProj	Mean of one minus the ratio between projected link length and projected link length limit for the FoF, *i.e.*, $\overline{1-(L_{link,rad}/L_{limit,rad})}$. Values from 0 to 1, with larger values meaning stronger links.	stat.correlation		double
LinkStrenZ	Mean of one minus the ratio between radial link length and radial link length limit for the FoF, *i.e.*, $\overline{1-(L_{link,rad}/L_{limit,rad})}$. Values from 0 to 1, with larger values meaning stronger links.	stat.correlation		double
LinkStrenComb	The average of LinkStrenProj × LinkStrenZ.	stat.correlation		double
RadKurt	Kurtosis of the projected radial distribution of galaxies, measured from IterCen.	stat.fit.param		double
VelSkew	Skewness of the distribution of galaxy velocities. Value of -999 if Nfof< 4.	stat.fit.param		double
VelKurt	Kurtosis of the distribution of galaxy velocities. Value of -999 if Nfof< 4.	stat.fit.param		double
Modality	Modality of the system, calculated as $(1 + VelSkew^2) / (3 + VelKurt^2)$.	stat.fit.param		double
AxAng	Angle of the group major axis on the sky using the Carter & Metcalfe (1980). Value of -999 if Nfof< 3.	pos.posAng	deg	
AxRat	Axial ratio of the minor and major axes of the group using the Carter & Metcalfe (1980) algorithm. Value of -999 if Nfof<3.	phys.size.axisRatio		
SymKS	Kolmogorov-Smirnov test of the uniformity of groups, after correction for the axial-ratio. Value of -999 if Nfof<3.	stat.probability		double
d3vol	3D convex hull volume of the group. Value of -999 if Nfof<4.	phys.volume	Mpc^3 h^{-3}	double
d3area	Surface area of the group hull. Value of -999 if Nfof<4.	phys.area	Mpc^2 h^{-2}	double
d2radec	Projected area of the group hull in the RA-Dec plane. Value of -999 if Nfof<3.	phys.area	Mpc^2 h^{-2}	double
d2raz	Projected area of the group hull in the RA-z plane. Value of -999 if Nfof<3.	phys.area	Mpc^2 h^{-2}	double
d2decz	Projected area of the group hull in the Dec-z plane. Value of -999 if Nfof<3.	phys.area	Mpc^2 h^{-2}	double
distortcirc	Measure of the circularity of the group in projection. Value of -999 if Nfof<3, equal or greater than 1 otherwise (distortcirc = 1 for a circle).	src.ellipticity		double
distortsph	Measure of the sphericity of the group. Value of -999 if Nfof<4, equal or greater than 1 otherwise (distortsph = 1 for a sphere).	src.ellipticity		double
distortellip	Measure of the ellipsoidicity of the group. Value of -999 if Nfof<4, equal or greater than 1 otherwise (distortellip = 1 for a ellipsoid).	src.ellipticity		double